

Retrieving soil surface roughness with the Hapke photometric model: Confrontation with the ground truth

S. Labarre, S. Jacquemoud, C. Ferrari, A. Delorme, A. Derrien, R. Grandin, M. Jalludin, François Lemaitre, Marianne Métois, Marc Pierrot-Deseilligny, et al.

▶ **To cite this version:**

S. Labarre, S. Jacquemoud, C. Ferrari, A. Delorme, A. Derrien, et al.. Retrieving soil surface roughness with the Hapke photometric model: Confrontation with the ground truth. Remote Sensing of Environment, 2019, 225, pp.1–15. 10.1016/j.rse.2019.02.014 . hal-02293285

HAL Id: hal-02293285
https://univ-lyon1.hal.science/hal-02293285

Submitted on 22 Oct 2021

HAL is a multi-disciplinary open access archive for the deposit and dissemination of scientific research documents, whether they are published or not. The documents may come from teaching and research institutions in France or abroad, or from public or private research centers.

L'archive ouverte pluridisciplinaire **HAL**, est destinée au dépôt et à la diffusion de documents scientifiques de niveau recherche, publiés ou non, émanant des établissements d'enseignement et de recherche français ou étrangers, des laboratoires publics ou privés.



Distributed under a Creative Commons Attribution - NonCommercial 4.0 International License

Version of Record: https://www.sciencedirect.com/science/article/pii/S0034425719300690
Manuscript_aac0aebfa92a161d32aede449e092023

Date: Friday, January 25, 2019
Title: Retrieving soil surface roughness with the Hapke photometric model: confrontation with the ground truth

Authors: S. Labarre[1], S. Jacquemoud[1*], C. Ferrari[1], A. Delorme[1], A. Derrien[2], R. Grandin[1], M. Jalludin[3], F. Lemaître[4], M. Métois[5], M. Pierrot-Deseilligny[6], E. Rupnik[6], B. Tanguy[4]

[1] Institut de physique du globe de Paris - Sorbonne Paris Cité, Université Paris Diderot, UMR CNRS 7154, 1 rue Jussieu, 75005 Paris, France (labarre@ipgp.fr; jacquemoud@ipgp.fr; ferrari@ipgp.fr; delorme@ipgp.fr; grandin@ipgp.fr)
[2] Observatoire Volcanologique du Piton de la Fournaise, Institut de physique du globe de Paris - Sorbonne Paris Cité, Université Paris Diderot, UMR CNRS 7154, 97418 La Plaine des Cafres, La Réunion, France (derrien@ipgp.fr)
[3] Centre d'Etude et de Recherche de Djibouti, BP 486, Djibouti, République de Djibouti (mohamed.jalludin@gmail.com)
[4] ONERA-DOTA - Université de Toulouse, 2 avenue Edouard Belin, BP 74025, 31055 Toulouse Cedex 4, France (francois.lemaitre@onera.fr; bernard.tanguy@onera.fr)
[5] Laboratoire de Géologie de Lyon - Université Lyon 1, ENS de Lyon, UMR CNRS 5276, 69100 Villeurbanne, France (marianne.metois@univ-lyon1.fr)
[6] Laboratoire en sciences et technologies de l'information géographique - IGN, ENSG, Université Paris-Est, 94160 Saint-Mandé, France (marc.pierrot-deseilligny@ensg.eu; ewelina.rupnik@ensg.eu)

[*] Corresponding author

Keywords: very high resolution digital elevation model; surface roughness; multiangular optical remote sensing; field goniometer; Pleiades satellite; Hapke photometric model; Bayesian inversion; Asal-Ghoubbet rift

Highlights:

- Multiangular reflectance and roughness are measured *in situ* on natural soils
- Multiangular reflectance is determined from Pleiades images
- A Bayesian inversion of the Hapke model is applied to both datasets
- Surface roughness retrievals are compared to the ground truth

Journal: *Remote Sensing of Environment*

Abstract

Surface roughness can be defined as the mean slope angle integrated over all scales from the grain size to the local topography. It controls the energy balance of bare soils, in particular the angular distribution of scattered and emitted radiation. This provides clues to understand the intimate structure and evolution of planetary surfaces over ages. In this article we investigate the capacity of the Hapke photometric model, the most widely used in planetary science, to retrieve surface roughness from multiangular reflectance data. Its performance is still a question at issue and we lack validation experiments comparing model retrievals with ground measurements. To address this issue and to

© 2019 published by Elsevier. This manuscript is made available under the CC BY NC user license
https://creativecommons.org/licenses/by-nc/4.0/

show the potentials and limits of the Hapke model, we compare the mean slope angle determined from very high resolution digital elevation models of volcanic and sedimentary terrains sampled in the Asal-Ghoubbet rift (Republic of Djibouti), to the photometric roughness estimated by model inversion on multiangular reflectance data measured on the ground (Chamelon field goniometer) and from space (Pleiades images). The agreement is good on moderately rough surfaces, in the domain of validity of the Hapke model, and poor on others.

1. Introduction

Surface roughness, which can be understood as a measure of the topographic relief of a bare soil, plays a key role in micrometeorology, hydrology, volcanology, geomorphology, planetary science and defense among others. It is a multiscale physical parameter which controls the energy balance, the scattering of incident radiation, and the directional emissivity of the ground, opening up the way for understanding its intimate structure and evolution over ages. Multiangular optical imagery is commonly used in planetary science to remotely provide a valuable information about roughness, a physical characteristic of soils that generates shadows at all scales. It is incorporated in photometric models through a shadowing function, with varying complexity. This function can be itself related to different characteristics of the boundary surface: ratio of mean hole depth-to-radius (Lumme and Bowell, 1981), mean slope angle of all the facets (Hapke, 1984), or fractal dimension (Shkuratov and Helfenstein, 2001). From a radiometric perspective, the shadowing function partly drives the shape of soil BRF (Bidirectional Reflectance Factor; Schaepman-Strub et al., 2006). However, the validation of these models on planetary bodies is indirect.

Models using other shadowing functions have been assessed on terrestrial surfaces (e.g., Cierniewski, 1987; Irons et al., 1992; Despan et al., 1999) but most of them have been validated only in the lab or in the field. All this work has opened up new perspectives to probe soil physical properties in the solar domain. On Earth, field measurements of surface roughness are pricy, difficult to implement and inefficient to cover large areas. Photogrammetric techniques now provide low-cost high-resolution surface topographic models, from which various statistical parameters can be derived

74 (e.g., Bretar et al., 2013; Gilliot et al., 2017). Remote sensing allows investigation of large or
75 inaccessible areas. Nonetheless scientists are still looking for a robust method to derive surface
76 roughness. For instance the interpretation of radar images ensuing from the direct link between the
77 backscattering coefficient and roughness remains relatively tricky. LiDAR is also a powerful tool for
78 analyzing soil topography but it is generally limited to the topographic scale.

79 To date the Hapke model is the most widely photometric model used in the scientific community
80 (Hapke, 2012). Although it gave rise to many improvements over the last thirty years, in particular
81 with regard to the physics of light-matter interaction, its formulation and the significance of its input
82 parameters are still debated. Nevertheless this model is simple and reproduces well the photometric
83 response of bare surfaces measured in the laboratory (e.g., Jacquemoud et al., 1992; Chappell et al.,
84 2006; Shepard and Helfenstein, 2007, 2011; Souchon et al., 2011; Beck et al., 2012; Pommerol et al.,
85 2013; Johnson et al., 2013), in the field (e.g., Pinty et al., 1989; Johnson et al., 2006a,b) or from space
86 (e.g., Wu et al., 2009; Ceamanos et al., 2013; Fernando et al., 2013; Vincendon, 2013; Sato et al.,
87 2014). To what extent multiangular imagery can inform us about soil roughness is, however, still a
88 pending question. The validation of the Hapke model, i.e., the comparison of the retrieved parameters
89 with the ground truth, still requires effort. Multiangular earth-orbiting satellites (e.g., MISR, Pleiades,
90 POLDER, Proba-1, SkySat) are designed to sample the directional reflectance over bare soils at
91 various spatial and spectral resolutions in the visible and near-infrared wavelengths. However, due to
92 the scarcity of concomitant *in situ* surface roughness and radiometric measurements, their ability to
93 retrieve soil roughness has not been demonstrated so far.

94 This article aims at estimating surface roughness on bare soils using the Hapke model from both
95 field and orbital photometric data, and to compare the retrieved values with *in situ* measurements
96 acquired in the Asal-Ghoubbet rift (Republic of Djibouti). First, we present the study site and *in situ*
97 measurements (section 2). Next, we expose the Pleiades satellite data after atmospheric correction and
98 cross calibration with field data (section 3). A Bayesian inversion of the Hapke model is performed on
99 both field and satellite data to estimate the photometric roughness of 12 sites and discuss the

coherence between the retrieved values (section 4). Finally, a discussion of the results is provided (section 5).

2. Field data

2.1. Study site

The Asal-Ghoubbet rift (Republic of Djibouti) is a young active rift. It began to form 900,000 years ago by extending the Somalia-Saudi plate boundary from the oceanic domain towards the west, to the triple point of Africa-Arabia-Somalia, currently located within the depression of Afar. It has been the subject of many research works in geophysics since the early 1970s because it allows small-scale study of the oceanic accretion above sea level (Fig. 1).

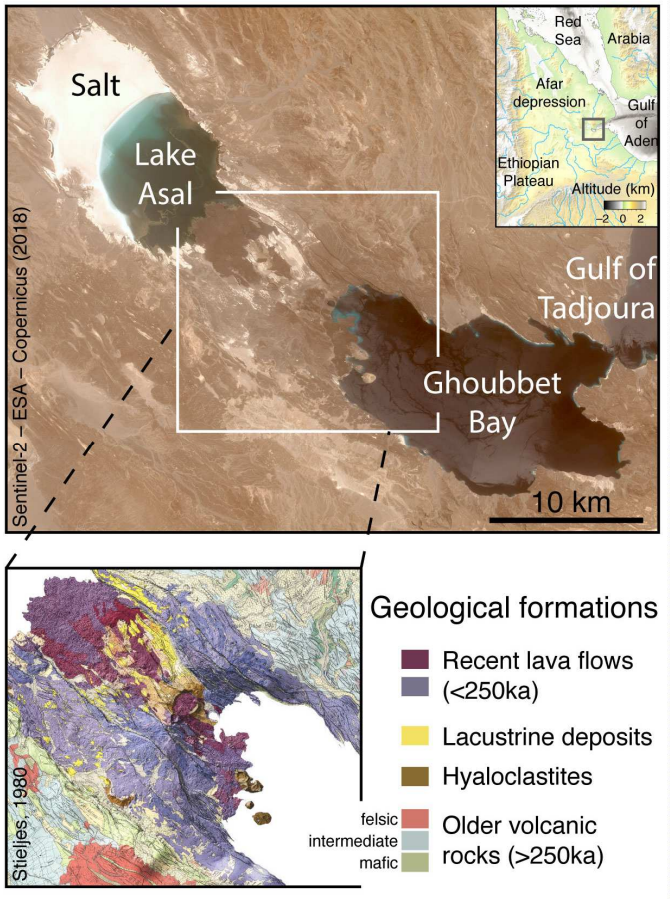


Fig. 1. Geographic context of the study site (11°35'N, 42°29'E). The image on top is a Sentinel-2 image of the Asal-Ghoubbet rift, Djibouti, acquired on 26 May 2018. The main water bodies and recent lava flows can be distinguished by their darker color, whereas recent sedimentary deposits (including salt deposits) have a brighter aspect. The bottom panel is a simplified geological map of the main area of interest targeted in this study (Stieljes, 1980, modified from Pinzuti et al., 2013).

112 This unique site meets the objectives of our study for two reasons:

113 1/ it displays a wide variety of bare soils over a small area (~100 km^2), from pure white salt
114 deposits to dark lava basalt flows, a contrasted topography, and a great wealth of surfaces, from
115 very rough lava flows to flat deposits in sedimentary basins (Fig. 2);

116 2/ it has a desert climate so that soils are marginally wet and sparsely vegetated. Because of the
117 presence of shoreline terraces generated during the formation of the rift, the lands are generally
118 homogeneous and flat.

119 A first exploratory mission has been conducted in April 2015 to identify areas of interest, and the
120 main campaign took place for two weeks in February 2016. Although organizing a field trip in this rift
121 is a challenge (desert area, strong winds, rudimentary infrastructure), it is easily accessible by car,
122 which makes it an ideal playground for our study.

123



Fig. 2. Twelve surfaces of increasing roughness studied in the Asal-Ghoubbet rift. From top left to bottom right, clay deposits (site F); reshaped hyaloclastic projections (site Y); lapilli deposits (site A); salt bank (site H); centimetric lava blocks (hyaloclastite) on lacustrine deposits (site E); slag on lacustrine deposits (site R); decimetric lava blocs on lacustrine deposits (site I); pulverulent limestone, rich in mollusc shells (site T); altered aphyric lava (site S); cracked lava crust (site M); basalt porphyry lava in the form of slabs (site Q); ropy pahoehoe lava (site B). See Caminiti (2000) for more information about the geomorphology of the rift.

124

125 ### 2.2. *In situ* roughness measurement

126 In order to determine the roughness parameter from the slope distribution of these terrains, the
127 topography has been reconstructed at the millimeter scale by means of UAV imaging.

128

129 #### 2.2.1. Topographic reconstruction at millimeter scale

130 Twenty two sites spanning over 30 m × 40 m areas have been surveyed using a quadcopter (DJI
131 F450) equipped with a flight control system, a compact-system camera (Sony Alpha 5100) and an
132 interchangeable lens (Sigma 30 mm F2.8). The quadcopter was maintained at a flight altitude between
133 8 m and 15 m to obtain a pixel size on the ground ranging from 1 to 2 mm. In this windswept region,
134 the camera settings (i.e., exposure time, aperture, and sensitivity) were adapted to each site so as to
135 provide correct image exposure. A camera calibration was also performed in the vicinity of the survey
136 area for maximum precision in the digital elevation model (DEM) reconstruction phase. To realize it,
137 a set of convergent images of a three-dimensional scene (rocks, buildings, etc.) was taken by hand
138 prior to each UAV acquisition.

139 The quadcopter was flown by an operator along parallel lines above the surface. Flight height
140 and path were controlled by real-time GNSS feedback on the aircraft position. An image overlap of
141 80% along the flight line and of 50% across the flight line was achieved by controlling the camera
142 automatic shooting time interval, the UAV speed and the trajectory. To geo-reference the images, five
143 ground control points designed to be easily identified in the UAV images were distributed
144 symmetrically across each measured site, and their geographical coordinates were measured with
145 dual-frequency GPS receivers (Ashtech Z-X) and their antennas (Ashtech Geodetic 4) at 1 Hz
146 sampling frequency. The accuracy of the position of these targets was estimated at approximating
147 1±0.7 cm (latitude), 0.4±0.3 cm (longitude) and 1.3±1.1 cm (altitude). In addition, wooden pieces of
148 defined dimensions (150 mm × 35 mm × 35 mm) were spread in the fields to provide three-
149 dimensional control information for *a posteriori* DEM validation.

150 The workflow to reconstruct the high resolution topography follows the steps described by
151 Bretar et al. (2013). It is based on MicMac, an open-source photogrammetric software

(https://micmac.ensg.eu/) (Pierrot-Deseilligny et al., 2006; Rupnik et al., 2017). About 12 out of 22 sites (A, B, E, F, H, I, M, Q, R, S, T and Y) have been processed to date on various reasons including wrong internal calibrations, overlapping problems, and time constraints. The spatial resolution of the DEMs ranges from 2.5 mm to 4 mm. Fig. 3 displays the shaded relief of four contrasted sites presented in Fig. 2. The planimetric accuracy is of the order of a few millimeters, while the relative vertical positional errors on the wooden pieces mentioned above are less than 3%.

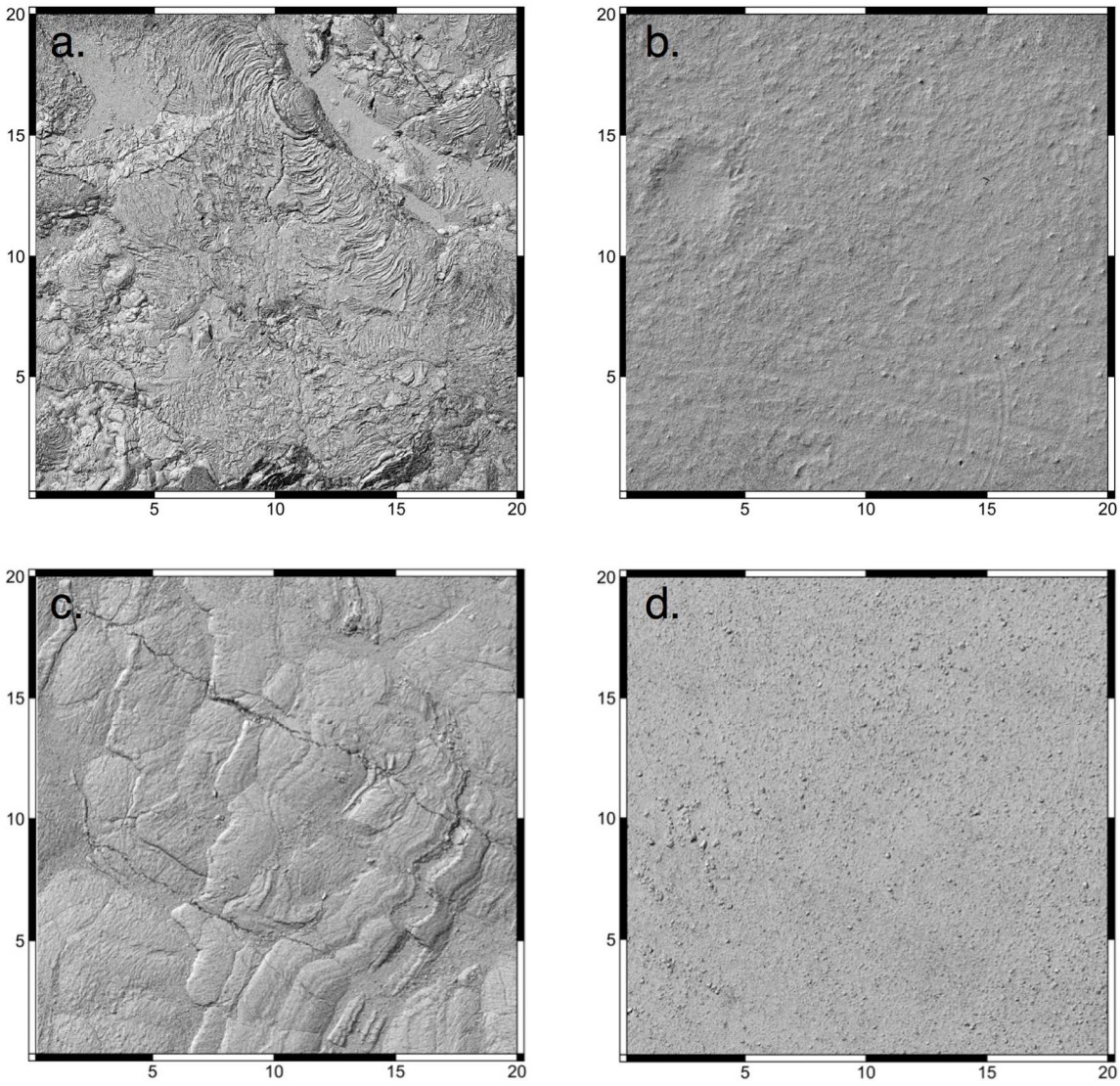


Fig. 3. 20 m long-sided areas extracted from shaded relief maps of digital elevation models for four remarkable sites of the Asal-Ghoubbet rift: sites (a) B, (b) F, (c) M, and (d) R. The spatial resolution of these four DEMs ranges from 2.8 mm to 3.2 mm.

2.2.2. Surface roughness determination

The mean roughness parameter $\overline{\theta}$ was computed using Eq. (1) (Labarre et al., 2017).

$$\tan\overline{\theta} = \frac{2}{\pi}\int_0^{\pi/2} a(\theta)\tan\theta\, d\theta \quad (1)$$

with θ being the slope angle of each facet of the surface and $a(\theta)$ the slope angle distribution. In order to compare the roughness between sites, a square 20 m on a side was first extracted from each DEM and then decomposed into twenty-five squares 4 m on a side to facilitate computations. The mean and the standard deviation of $\overline{\theta}$ calculated for the 12 sites are given in Table 1 and the slope distributions are illustrated in Fig. 4. The slopes of the two smoothest sites, F and Y, are less than 50°. Sites E and R show similar distributions. The distribution of site B and site Q reveals very few values greater than 70° because they present little discontinuities. Sites M and S have the same roughness and similar distributions, except that the amplitude at angles higher than 50° is stronger for site S due to the presence of pebbles and centimeter blocks on the surface. The roughness of sites B, A and Y is comparable to that found in the Piton de La Fournaise for similar terrains (Bretar et al., 2013; Labarre et al., 2017).

Site	Latitude N	Longitude E	Description	$\overline{\theta}$	SD
A	11.5810209904	42.4930719598	Lapilli deposits	18.6	±2.1
B	11.5945984130	42.4726550328	Ropy pahoehoe lava	33.4	±5.1
E	11.5936487248	42.4917893931	Centimetric lava blocks (hyaloclastite) on lacustrine deposits	23.1	±2.9
F	11.5925120813	42.4958721760	Clay deposits	8.3	±1.7
H	11.6199221528	42.3965061773	Salt bank	20.9	±2.2
I	11.5633683315	42.4485707122	Decimetric lava blocs on lacustrine deposits	27.9	±2.4
M	11.5896442760	42.5030110060	Cracked lava crust	18.3	±1.9
Q	11.5618838898	42.5136321246	Basalt porphyry lava in the form of slabs	33.1	±4.2
R	11.5361663318	42.4923411655	Slag on lacustrine deposits	23.1	±1.3
S	11.5416993639	42.4811000172	Altered aphyric lava	18.3	±2.6
T	11.5585832484	42.4558691802	Pulverulent limestone, rich in mollusc shells	20.9	±2.6
Y	11.5864054883	42.4881465853	Reshaped hyaloclastic projections	12.6	±2.0

Table 1. Geographical coordinates, geological description, mean roughness $(\overline{\theta})$ and standard deviation (SD) of 12 sites. The values of $\overline{\theta}$ and SD expressed in degrees are calculated over 25 tiles of 16 m^2 each.

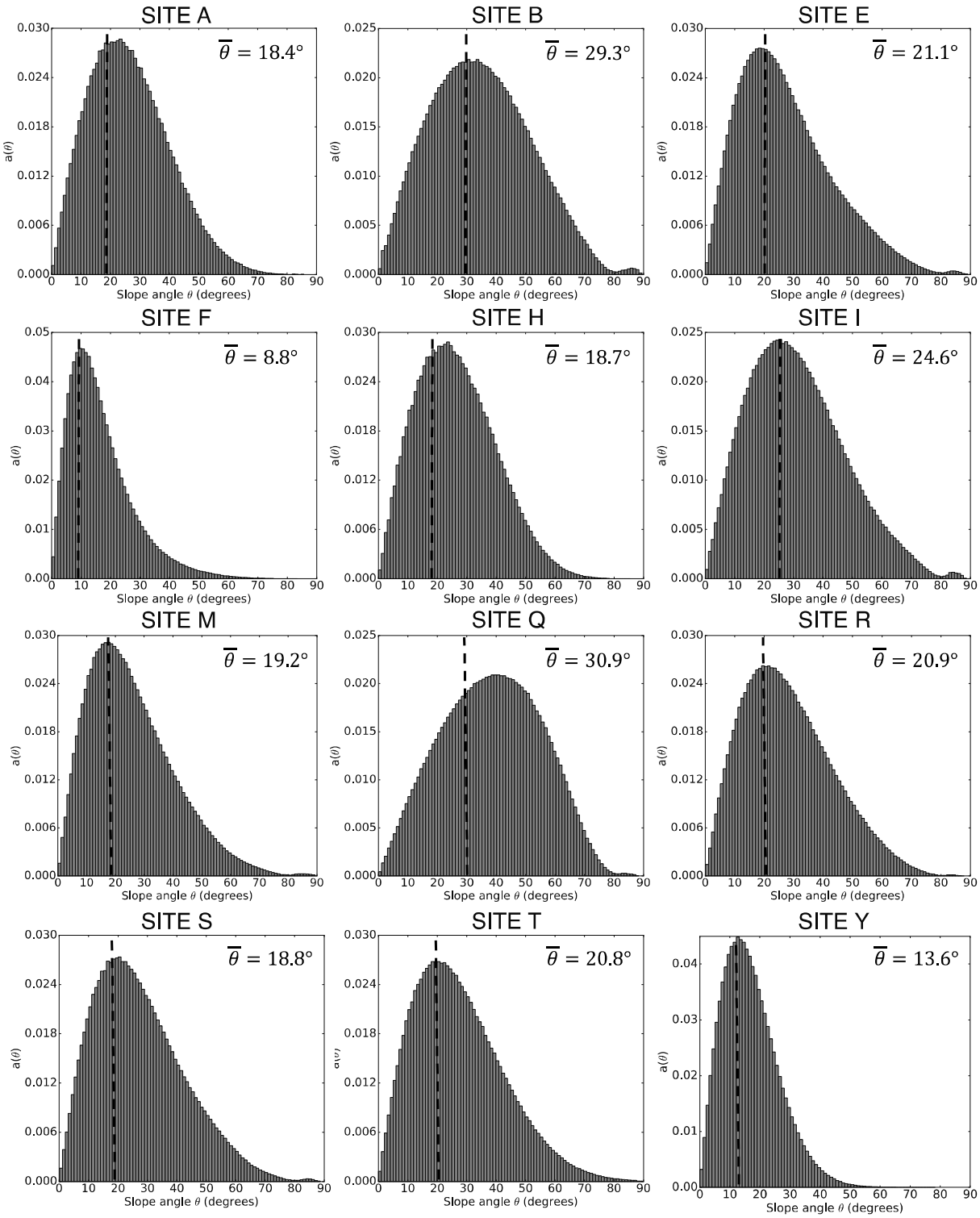


Fig. 4. Slope distribution evaluated on one tile representative of the twelve sites introduced in Fig. 2. The dashed lines correspond to the roughness values $\overline{\theta}$ determined using Eq. 1. Note that the values indicated in each panel are slightly different from those displayed in Table 1, which are averages of 25 tiles.

177

178 **2.3. *In situ* multi-angular photometric measurements**

179 In order to estimate the photometric roughness with the Hapke model at microscopic and
180 mesoscopic scales, the bidirectional and spectral radiances were measured in the field over 10 of the
181 selected soils (A, D, E, F, H, M, O, Q, R, and T) with the Chamelon, a new portable field goniometer

system designed by ONERA (Toulouse, France) to record the hemispherical conical reflectance factor and coupled with a FieldSpec 4 spectroradiometer (ASD Inc.). They are both remotely controlled by an in-house developed software and mounted on a cart equipped with wheels to facilitate movement. Such outdoor measurements that developed in recent years are still challenging (e.g., Sandmeier, 2000; Doctor et al., 2015; Bachmann et al., 2016; Furey, 2016; Harms et al., 2016). The remoteness of the Asal-Ghoubbet rift, strong winds and high temperatures during the fied experiment made things even more difficult.

A four-axis articulated arm allowed to perform directional measurements. The radiance of each targetted field was measured using a fixed 8° instantaneous field-of-view (IFOV): this corresponds to a disk of about 20.56 cm in diameter at nadir, assuming a conical view and a distance to the target of 147 cm. This footprint changes to an ellipse with increasing viewing angle: it is four time bigger at a 60° viewing angle. The measurements are made according to the following protocol (Fig. 5): the Chamelon is facing the sun; the solar zenith angle i is calculated knowing the Julian day, the universal time, the latitude and longitude of the site; the articulated arm moves in five measurement planes: two principal planes of the Sun (left and right side), one perpendicular plane, and two 45° planes (left and right side). The radiance of the ground is acquired in thirteen viewing directions e from −59.11° to +59.09° in each of the five planes, and in-between, the radiance of a Spectralon reference panel (Labsphere) is acquired at nadir. At the end of an acquisition cycle, the arm circularly moves around the device to sample the surface at nadir. A complete cycle thus represents 103 measurements: 7 vertical measurements on the Spectralon panel, 5×13 directional measurements and 15+16 vertical measurements.

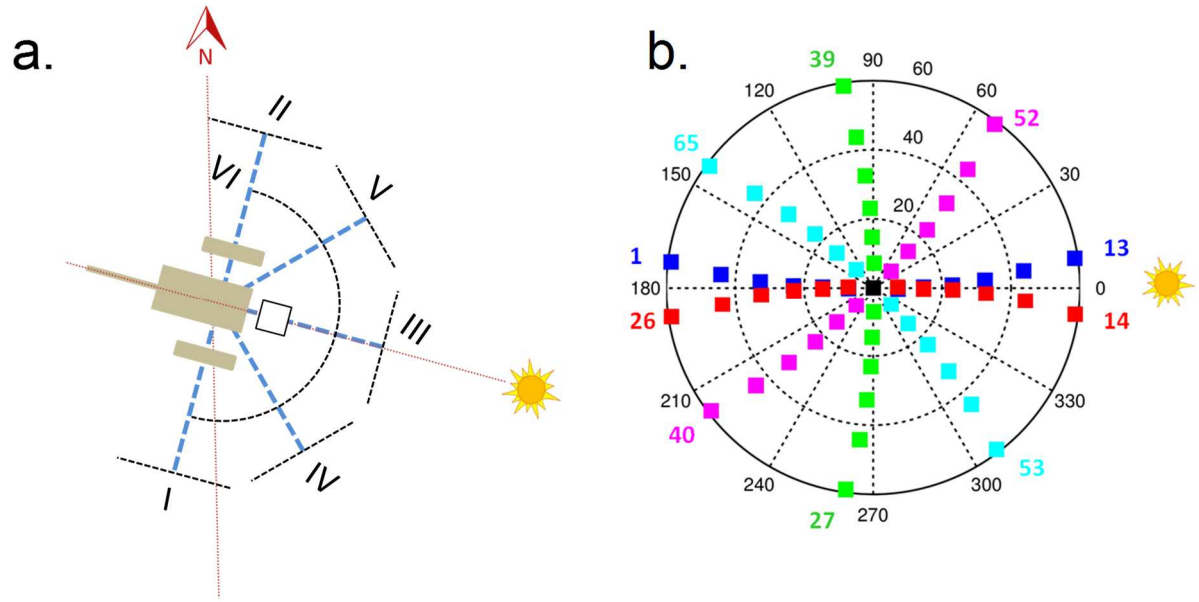


Fig. 5. (a) Measuring planes of the Chamelon field spectro-goniometer: (I) right principal plane of the Sun, (II) left principal plane of the Sun, (III) perpendicular plane, (IV) oblique plane at 45° azimuth on the right, (V) oblique plane at 45° azimuth on the left, and (VI) circular sight. (b) Sampled viewing directions: main plane on the right (blue), main plane on the left (red), perpendicular plane (green), oblique plane at 45° azimuth on the right (magenta), oblique plane at 45° azimuth on the left (cyan). The numbers from 1 to 65 indicate the order of the directional measurements.

A cycle approximately lasts 17 min whereas the sun zenith and azimuth angles are likely to vary from 0.43° to 4.81° and from 0.83° to 9.32°, respectively, depending on the time of the day. Variations in sun zenith angle are more important early in the morning and late in the afternoon. Conversely, variations in solar azimuthal angle are maximum around noon. Such variations are not inconvenient for the inversion of the Hapke model, because the illumination and viewing angles are exactly known for each measurement.

In order to appraise the spatial variability of the bidirectional reflectance factor, between two and six positions were sampled within each site by moving the Chamelon a few meters. For portability reasons, and since the size of the smallest area measured on the ground must be statistically representative of the site, the rougher terrains have not been measured.

The radiance of the Spectralon panel measured at close intervals is used to determine the BRF of the soils, but also to detect instrumental drifts or to remove data affected by clouds. Fig. 6a shows the reflectance of site A measured between 400 nm and 2500 nm in six viewing directions, symmetrical with respect to the principal plane of the Sun. Ideally, they should be paired: this is the case in the directions 1 and 26 (principal planes of the Sun I and II in the forward direction) and in the directions

27 and 39 (perpendicular plane III), but not in the directions 13 and 14 (principal planes of the Sun I and II in the backward direction). The fact that the Chamelon targets different spots during the acquisition cycle is certainly the cause of the discrepancy that is greater in the backward direction due to the hotspot effect. Fig. 6b displays the BRF of the same site in the visible. The asymmetry observed in the hot spot direction is a consequence of the difference of reflectance measured between the directions 13 and 14.

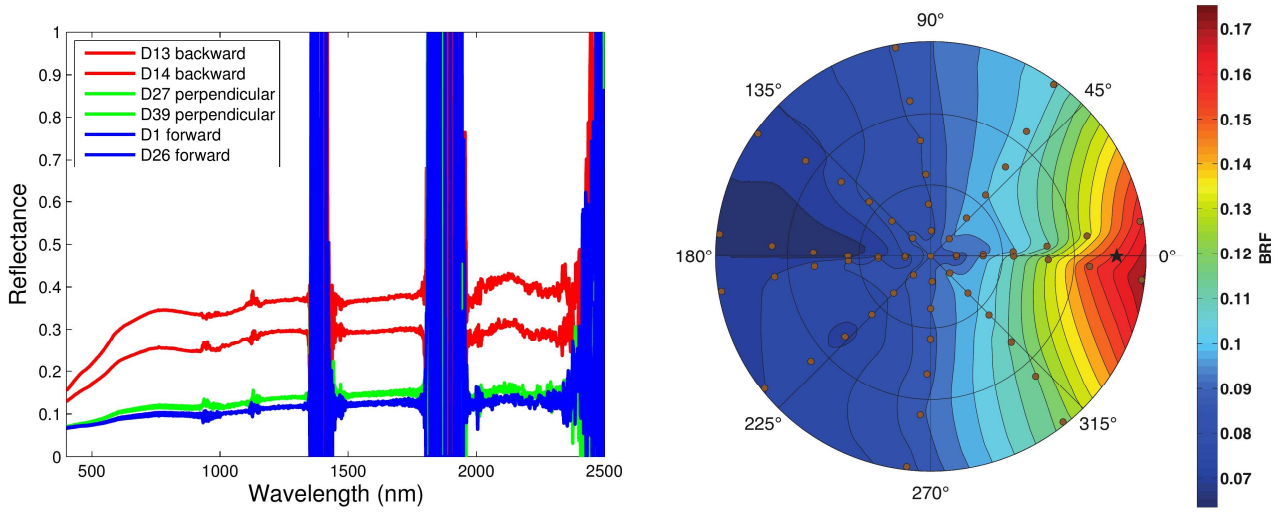


Fig. 6. (left) Reflectance spectra of site A for six viewing directions as described in Fig. 5a. The noisy values around 1400 nm, 1900 nm, and 2500 nm are located in spectral regions where atmospheric water vapor strongly absorbs radiation. (right) Bidirectional reflectance factor of site A averaged over the panchromatic band of Pleiades (see Fig. 7c).

3. Satellite data

The agility of the Pleiades satellite allows unique measurements of the ground BRF at macroscopic scale. A sensitivity analysis demonstrates the impact of the aerocol optical thickness on the observed BRF. Cross-calibration with the Chamelon data improves the atmospheric correction by fixing the other important factor impacting the correction, i.e., the adjacency radius.

3.1. Pleiades images

The Pleiades 1A and 1B satellites, launched in December 2011 and December 2012 respectively, operate on the same quasi-circular orbit at an altitude of 694 km and they are 180° out of phase. They aim to image the surface of the Earth in the visible-near infrared wavelengths with both a 50 cm

spatial resolution in panchromatic mode and a 2 m spatial resolution in multispectral mode (blue, green, red, and near infrared) (Fig. 7c). In addition to a high spatial resolution, they offer exceptional agility that allows rapid off-nadir acquisitions up to ~50°, thus offering many different observation geometries (Gleyzes et al., 2012; Lachérade et al., 2012). One can take advantage of this property to produce high resolution DEMs (Rupnik et al., 2018). During the in-orbit commissioning phase of the Pleiades 1B satellite conducted by CNES (Centre national d'études spatiales), a series of twenty-one multiangular images were acquired in video mode in a single flyby of the Asal-Ghoubbet rift on January 26, 2013 (Figs. 7a,b). The total acquisition time was about four minutes, from 7:49:18 UTC to 7:53:27 UTC. The swath along the orbital track varied from ~20 km at nadir to ~60 km at grazing angle. The high resolution multi-angular reflectances acquired with a large angular sampling over a wide range of surfaces in terms of color, roughness and mineralogical properties, is unique.

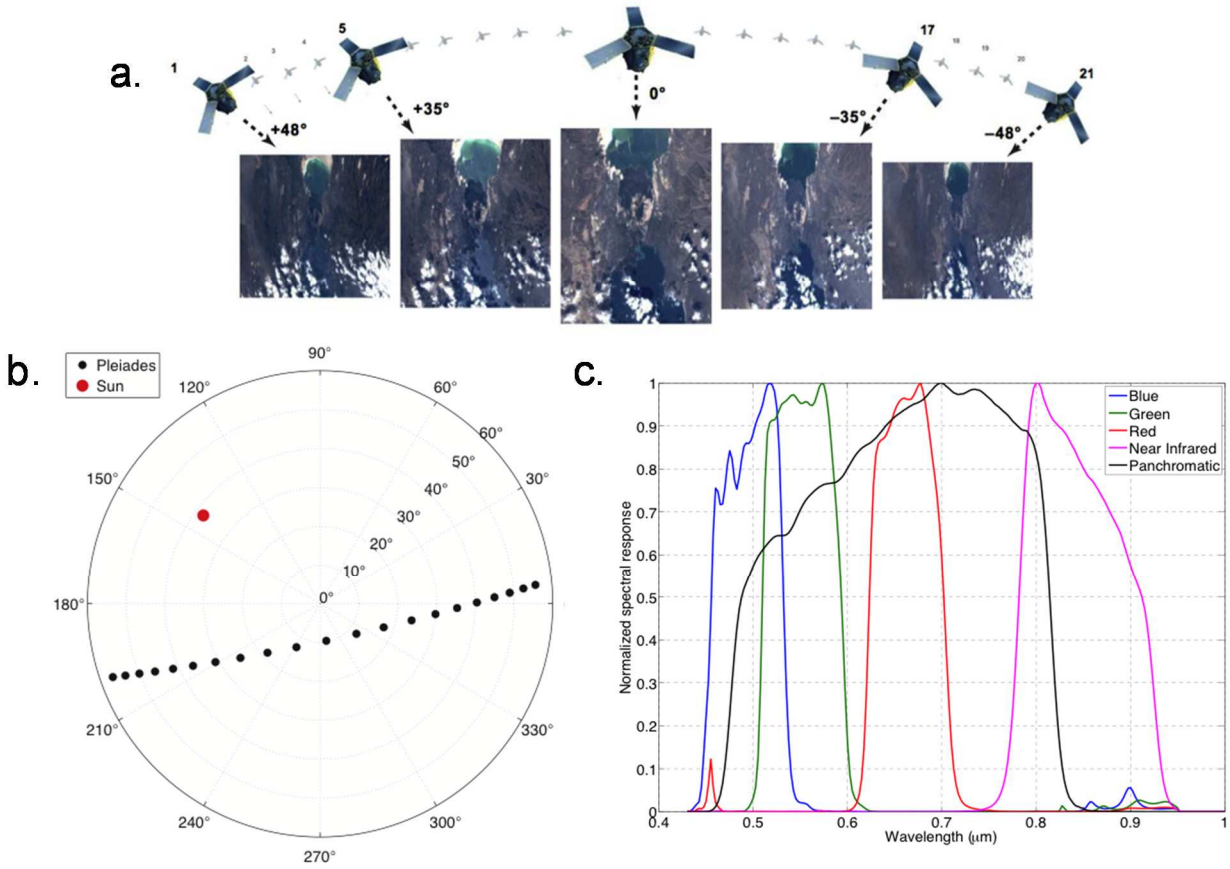


Fig. 7. (a) Visual representation of the Pleiades video acquisition; (b) Observing geometry of the studied zone: the black dots indicate the viewing directions and the red disk the position of the Sun in an azimuth-elevation projection; (c) Normalized spectral bands of the Pleiades satellite (Lachérade et al., 2012).

3.2. Atmospheric corrections

The atmospheric correction of the 21 Pleiades images is a critical step impacting the shape of the BRF, therefore the accuracy of the retrieved surface roughness. It is based on the 6S radiative transfer code (Vermote et al., 1997) which is implemented in the Orfeo ToolBox library (OTB, https://www.orfeo-toolbox.org/), a set of algorithmic bricks and satellite image processing utilities developed by CNES and designed to process the Pleiades images (Fig. 8). Four atmospheric parameters have to be provided using ancillary datasets: the atmospheric pressure P_a, the water vapor content U_{H_2O}, the ozone content U_{O_3}, and the aerosol optical thickness τ_A. They were all determined over Djibouti on January 26, 2013.

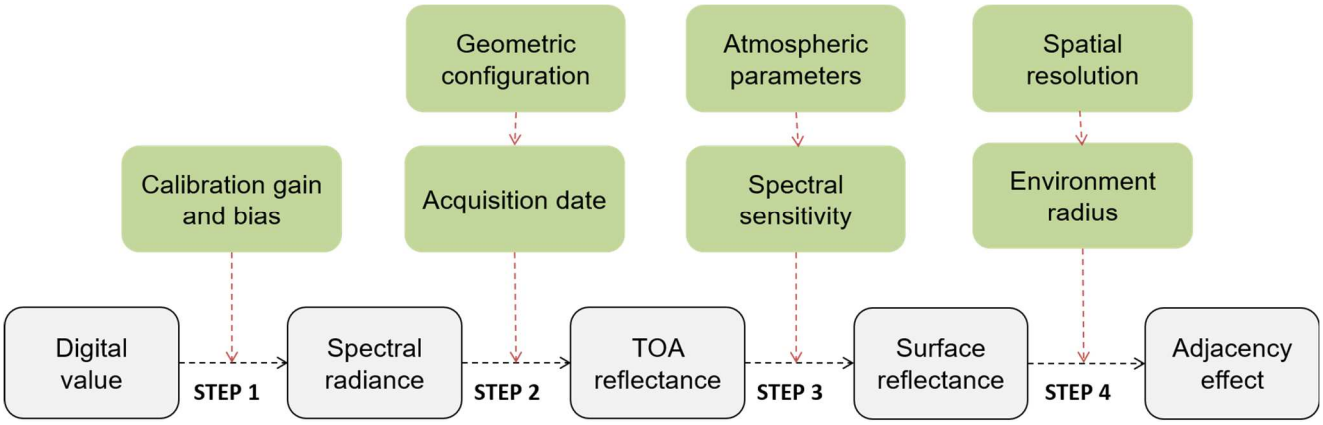


Fig. 8. Orfeo ToolBox (OTB) processing chain for radiometric calibration of the Pleiades images. The white frames represent the steps and the green frames the input parameters.

Atmospheric pressure and ozone content do not vary much spatially and temporally, so they can be estimated from low spatial resolution meteorological data. On the contrary, water vapor and aerosol content are highly variable so the calibration requires data with high temporal and spatial resolution. In the absence of atmospheric measurements as the satellite flew over the Asal-Ghoubbet rift, the aerosol optical thickness was provided by the MODIS (*Moderate Resolution Imaging Spectrometer*) instrument onboard the AQUA satellite: $\tau_A = 0.22$. The water vapor content was also derived from the MODIS instrument onboard the TERRA satellite: $U_{H_2O} = 2.325\ g.cm^{-2}$. The column ozone content has been derived from the OMI (*Ozone Monitoring Instrument*) spectrophotometer onboard the AURA satellite: $U_{O_3} = 244$ DU. Finally, the Global Modeling and Assimilation Office that supports

NASA's Earth Science mission uses the GEOS-5 atmospheric data assimilation model to build a consistent temporal database for sea level atmospheric pressure: $P_a = 1014.72$ hPa.

The 6S code computes four radiometric quantities in the solar domain between 400 nm and 2500 nm: the intrinsic reflectance and the spherical albedo of the atmosphere, the total gaseous transmission, and the total transmittance of the atmosphere along both the sun-surface and surface-satellite optical paths. To take into account the adjacency effect, the average reflectance from contiguous pixels within a circle of radius r around the target pixel is calculated and a correction is made (Appendix A). The processing chain leading to the surface reflectance of the region of interest is applied to the 21 images separately, and the region of interest is then projected onto each sensor geometry as a polygon. The bidirectional reflectance value at a given viewing angle is the mean value of the pixels included in the resulting polygon and the error is the confidence interval at 95%.

3.3. Sensitivity of bidirectional reflectance to atmospheric parameters

As mentioned earlier, the shape of the BRF is of critical importance to the retrieval of accurate surface roughnesses. In order to quantify the impact of atmospheric corrections on the calculation of surface reflectance, a one-factor-at-a-time sensitivity analysis of the atmospheric parameters was carried out on two zones selected on criteria of color and roughness (Fig. 9): zone 1 is a silty, flat and bright surface while zone 2 is basalt, rough and dark lava flow. The reflectance factor is first calculated at ground level using the default parameter set implemented in the OTB: $U_{O_3} = 0$ DU, $U_{H_2O} = 2.5\ \mathrm{g.cm^{-2}}$, $P_a = 1030$ hPa, $\tau_A = 0.2$, desert aerosol model, and no adjacency effect correction.

The effect of water vapor is limited to a modulation of the amplitude of the reflectance. It is reduced in the visible with variations less than 5%, and notable in the near infrared beyond 700 nm due to the presence of weak absorption bands. The ozone content has a larger impact in the visible, in particular in the green band of Pleiades covering the Chappuis band between 550 nm and 650 nm, and has no effect in the near infrared. The influence is important at grazing angles, which results in a significant deformation of the multi-angular reflectance. The atmospheric pressure has a relative

298 impact of less than 5%. Like water vapor, it acts as a scaling factor and is not critical to the correction
299 of the reflectance. Conversely, one can observe a strong influence of aerosol optical thickness on the
300 shape of the reflectance distribution, especially in zone 2 which is darker. The difference with the
301 reference distribution can reach 100% for extreme values, and it tends to increase with the viewing
302 angle or towards shorter wavelengths. Finally, extending the adjacency radius changes both the
303 amplitude and the shape of the reflectance distribution. Therefore, the two most influential
304 atmospheric parameters critical for the determination of soil roughness are the aerosol optical
305 thickness and the adjacency radius.
306

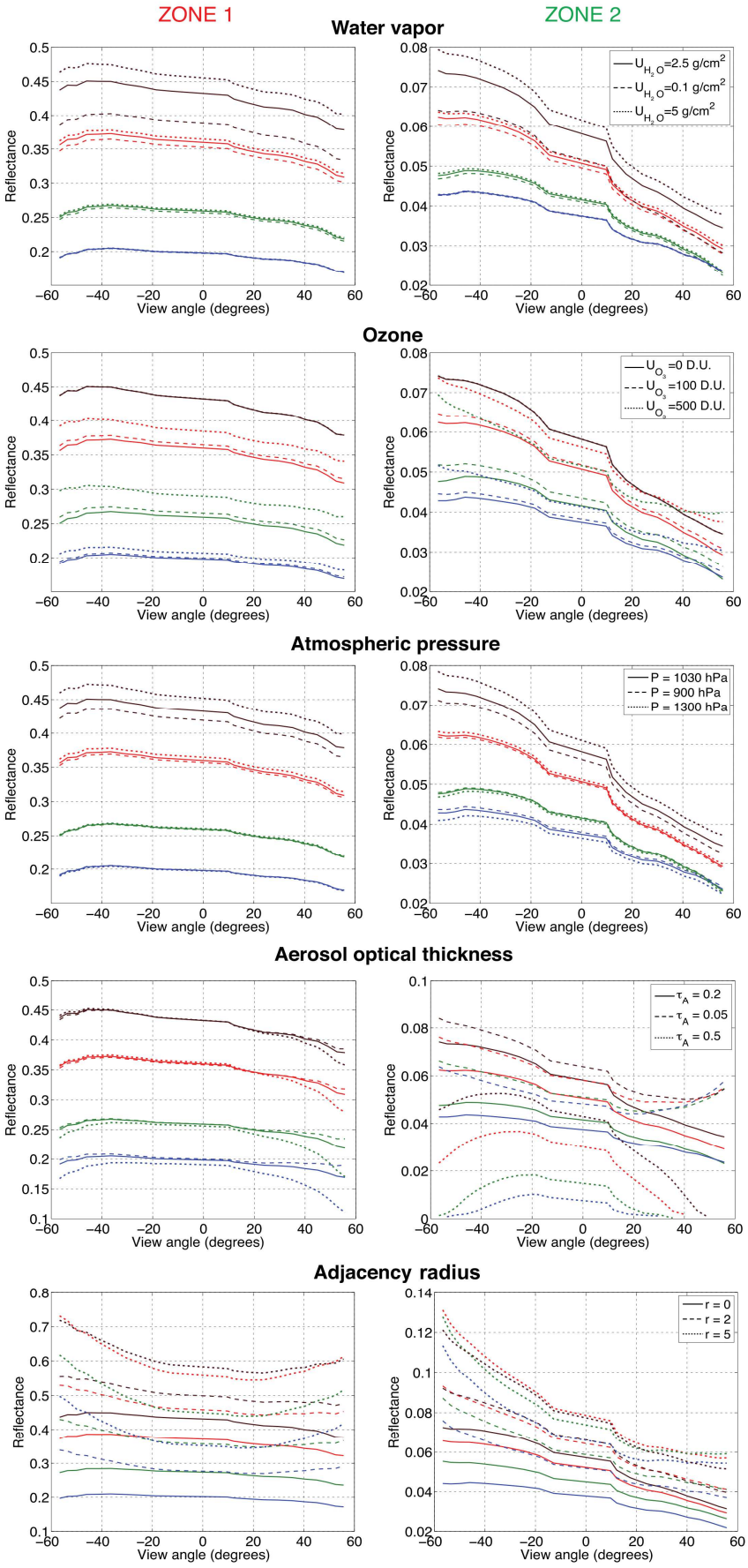


Fig. 9. Determination of the bidirectional reflectance factor (BRF) of two contrasted zones (left/right) in the four Pleiades bands (R: red lines, G: green lines, B: blue lines, PIR: black lines) along the acquisition geometry (Fig. 3) for the default parameters set (solid line) and high (dotted line) and low (dashed line) values of the parameters of the atmospheric correction. The adjacency radius r is expressed in pixel.

3.4. Cross-calibration between Pleiades and Chamelon measurements

In situ measurements conducted in the Asal-Ghoubbet rift were used as ground truth to check and to adjust the quality of the orbital measurements. We superimposed the Pleiades reflectances acquired in four spectral bands and at 21 viewing angles on the Chamelon reflectances acquired from 400 nm to 900 nm and at 65 viewing angles. Fig. 10 displays the reflectance factor ratio relative to the green band, chosen arbitrarily, for sites F (clay deposits), M (decimetric lava blocs on crust), and T (pulverulent limestone) and two adjacency radii ($r = 0$ and $r = 1$). The agreement is best when $r = 1$ so we used this value to extract the photometric curves of the Pleiades images. On applying this correction the reflectance as derived from Pleiades tends to decrease in the near infrared down to a lower value than in the red (Fig. 10). This effect is greater for site M, the spectral signature of which is typical of lunar basalts (e.g., Staid, 2000; Antonenko and Osinki, 2010).

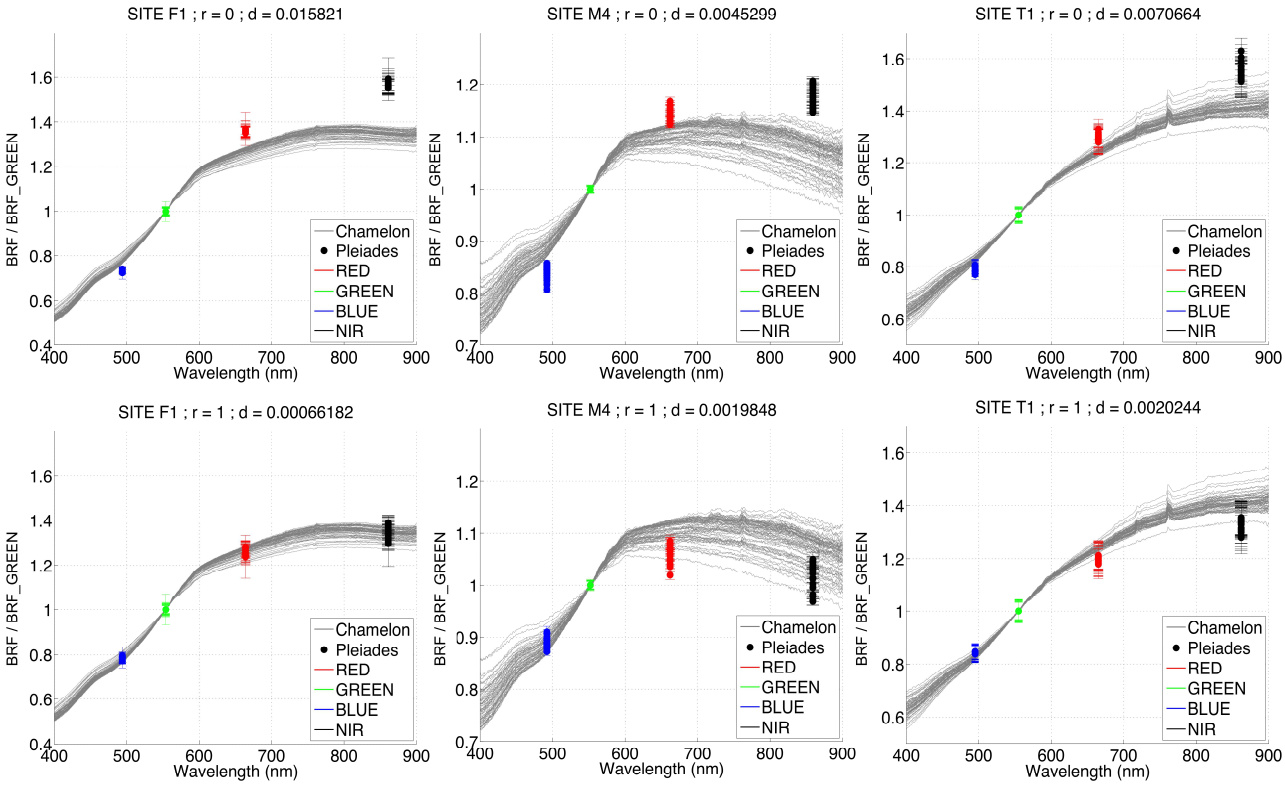


Fig. 10. Comparison between the ratio to the green band of the bidirectional reflectance factor (BRF) spectra for the Chamelon (gray curves) and Pleiades (colored dots) for different values of the adjacency effect radius ($r = 0$ at the top; $r = 1$ at the bottom) and for the sites F (left), M (middle) and T (right) of the Asal-Ghoubbet rift.

3.5. Pleiades multiangular reflectance

Fig. 11 illustrates the bidirectional reflectance factor (BRF) extracted over 12 sites in the four spectral bands of the Pleiades satellite after calibration. The average albedo of sites F (clay deposits), T (pulverulent limestone) and H (salt bank) changes from bright to very bright. The shape of the BRF versus the viewing angle of site H is slightly convex, whereas that of site F is flat and collapses at grazing viewing angles. Site T exhibits a negative slope. The shape and magnitude of the BRF of the other sites are similar in the four spectral bands, except at site R for which some points are missing due to the presence of clouds and shadows, and sites B and Q that display lower amplitude. The BRF of sites A, S and Y is similar despite different surface features. The roughest surfaces of sites B and Q are also comparable. At first glance, on can note that the Pleiades BRF does not vary much in shape and that the albedo seems to be a more robust segmentation criterion.

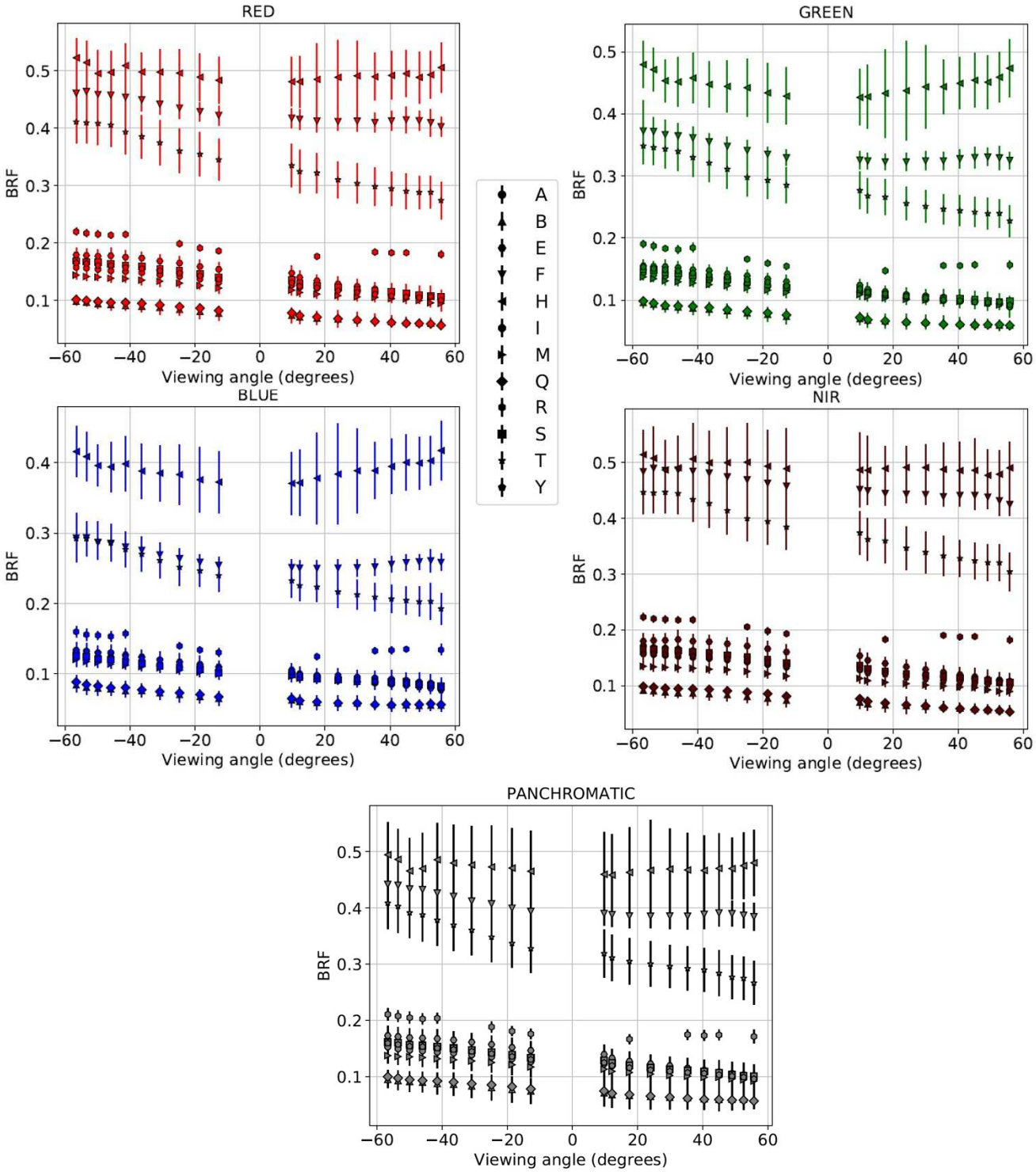


Fig. 11. Bidirectional reflectance factor (BRF) measured by Pleiades at twelve sites of the Asal-Ghoubbet rift in the four spectral bands and the panchromatic band of the sensor. By convention, the negative viewing angles correspond to azimuth angles ranging from 90° to 270° (Fig. 7b).

4. Results on soil roughness

In this section we examine whether the mean surface roughness derived from very high resolution DEMs is consistent with the photometric roughness retrieved by inversion of the Hapke model on soil multiangular reflectance data acquired at centimeter and meter scales.

338

339 **4.1. The Hapke model**

340 The bidirectional reflectance factor of a particulate medium can be calculated using the radiative
341 transfer model developed by Hapke (1981). The latest version that considers the porosity correction is
342 written as (Hapke, 2008):

343

$$\pi r_R(i,e,g) = \frac{K(P)}{\mu_0}\frac{w}{4}\frac{\mu_{0e}}{\mu_{0e}+\mu_e}\left[p(g,b,c)B_S(B_0,P,g) + M(w,\mu_{0e},\mu_e)\right]S\left(i,e,g,\overline{\theta_H}\right) \quad (2)$$

344

345 with $K(P)$ the porosity coefficient related to the porosity P of the medium, w the single-scattering
346 albedo (ratio of scattering coefficient to total extinction coefficient), i and e the illumination and
347 viewing angles, respectively ($\mu_0 = \cos i$ and $\mu = \cos e$), $p(g,b,c)$ the phase function for the phase
348 angle g and the phase function parameters b (anisotropy parameter) and c (backscattering coefficient),
349 B_S the function describing the shadow-hiding opposition effect (SHOE) and depending on the
350 parameter B_0, named opposition surge amplitude, M a function modeling multiple scattering, and S a
351 shadowing function quantifying the effects of the photometric roughness $\overline{\theta_H}$ (Appendix B). μ_{0e} and
352 μ_e are the cosines of the effective illumination and viewing angles, the expressions of which depend
353 on $\overline{\theta_H}$.

354

355 **4.2. Photometric roughness**

356 Many authors have inverted the Hapke model by using conventional non-linear least squares
357 methods but the parameter uncertainties have been seldom, if ever, determined (e.g., Jacquemoud et
358 al., 1992; Gunderson et al., 2006; Shepard and Helfenstein, 2007; Wu et al., 2009; Helfenstein and
359 Shepard, 2011). Fernando et al. (2015) and Schmidt and Fernando (2015) recently demonstrated the
360 relevance of a probabilistic inversion to estimate the photometric parameters of the model over Mars.
361 We followed their approach on the Pleiades and Chamelon reflectances.

362 The complete Hapke model depends on six parameters (w, $\overline{\theta}$, B_0, P, b and c) for which no prior

information is available. A uniform probability density function (PDF) is thus considered over their range of variation. Outside this range, the PDF equals zero to discard nonphysical solutions. A global sensitivity analysis of the model recently performed by Labarre et al. (2017) confirmed that the opposition surge amplitude B_0 did not influence the estimation of the other parameters, which was suspected by other authors (e.g., Wu et al., 2009; Fernando et al., 2013). However we left it free during the inversion insofar as the calculation time was not significantly affected. The inversion of the model was performed using the Python PyMC library (Patil, 2010) that implements Bayesian statistical models and fitting algorithms, including Markov Chains Monte Carlo. The retrieved values of the parameters are the median of the *a posteriori* PDF provided by PyMC, and the uncertainties corresponds to the 95% confidence interval. The inversion is a two-stage process: first synthetic tests are carried out in different geometrical configurations; second the model is inverted on the Pleiades and Chamelon data. Only three parameters are likely to be accurately constrained by inversion from the observations: w, $\overline{\theta_H}$ and b.

Since the grain size is assumed to be larger than the wavelength (a major hypothesis of the model), the roughness and the phase function parameters are assumed to be wavelength independent. Same with the porosity and the opposition effect parameter, the influence of which on the model is small. Therefore, the single scattering albedo, which is related to the optical constants of the constituting materials of the medium, is the only wavelength-dependent parameter. Because of the interactions between w and some parameters (Labarre et al., 2017), their estimated values may vary with wavelength, although this is physically meaningless.

The inversion of the Hapke model was first conducted both on the spectral (R, G, B and NIR) and the panchromatic (P) bands of Pleiades. In total 21 viewing angles were available for the 12 sites except for site R where the number of observations was reduced to 13 due to the presence of clouds in some images. Although the preliminary tests revealed a deterioration in the estimation of the photometric parameters as the number of observations decreased, the constraint on the parameters remained good on this site. Assuming that only w varies spectrally, we also inverted the model on the four spectral bands simultaneously, as suggested by Jacquemoud et al. (1992), Chappell et al. (2006)

and Wu et al. (2009). This led to the retrieval of 9 parameters: the four single scattering albedos (w_R, w_G, w_B and w_{NIR}), the photometric roughness ($\overline{\theta_H}$), the two phase function parameters (b and c), the porosity (P) and the opposition surge amplitude (B_0). By providing better observational constraints, the quality of the retrieval is generally improved. Without information on the uncertainty associated with the Chamelon observations, we fixed it to 10% of the observed values. Although between two and six complete BRFs are available in each site, we inverted the Hapke model on only one chosen on the basis of the stability of atmospheric conditions, the homogeneity of the surface, and the symmetry of the BRF with respect to the principal plane of the Sun. The Chamelon spectra were convoluted by the filter functions of the Pleiades sensor displayed in Fig. 3c to obtain spectrally homogeneous data. The retrieved values of $\overline{\theta_H}$, the parameter of interest, are gathered in Table 2 and Figure 12. The single scattering albedo w is added to check consistency of the Chamelon-Pleiades cross-calibration.

Site	Sensor	Photometric roughness $\overline{\theta_H}$		Single scattering albedo w				
		P	MS	P	B	G	R	NIR
A	Pleiades	21.1 ± 16.1	21.9 ± 3.2	0.34 ± 0.17	0.26 ± 0.09	0.29 ± 0.11	0.33 ± 0.12	0.34 ± 0.12
	Chamelon	25.8 ± 6.8	24.7 ± 3.7	0.33 ± 0.15	0.28 ± 0.10	0.37 ± 0.12	0.37 ± 0.12	0.39 ± 0.12
B	Pleiades	28.5 ± 27.2	19.9 ± 16.2	0.30 ± 0.26	0.22 ± 0.09	0.24 ± 0.10	0.25 ± 0.10	0.24 ± 0.10
E	Pleiades	33.7 ± 23.6	29.2 ± 6.5	0.46 ± 0.29	0.33 ± 0.12	0.38 ± 0.13	0.43 ± 0.14	0.44 ± 0.15
	Chamelon	30.5 ± 7.3	30.7 ± 3.6	0.40 ± 0.18	0.31 ± 0.14	0.35 ± 0.15	0.43 ± 0.17	0.46 ± 0.17
F	Pleiades	24.8 ± 15.8	27.1 ± 5.2	0.86 ± 0.13	0.43 ± 0.69	0.79 ± 0.13	0.88 ± 0.11	0.90 ± 0.09
	Chamelon	19.5 ± 3.4	18.9 ± 2.4	0.93 ± 0.04	0.81 ± 0.04	0.88 ± 0.04	0.94 ± 0.03	0.95 ± 0.02
H	Pleiades	14.8 ± 14.7	22.5 ± 14.5	0.89 ± 0.16	0.86 ± 0.13	0.90 ± 0.11	0.93 ± 0.10	0.93 ± 0.10
	Chamelon	22.2 ± 5.7	21.6 ± 2.7	0.93 ± 0.05	0.88 ± 0.03	0.91 ± 0.03	0.94 ± 0.02	0.96 ± 0.02
I	Pleiades	31.8 ± 22.0	30.6 ± 8.6	0.44 ± 0.28	0.35 ± 0.15	0.39 ± 0.16	0.43 ± 0.17	0.43 ± 0.17
M	Pleiades	32.1 ± 21.6	28.3 ± 4.5	0.40 ± 0.27	0.32 ± 0.12	0.35 ± 0.13	0.37 ± 0.13	0.36 ± 0.13
	Chamelon	40.8 ± 5.0	41.5 ± 3.5	0.28 ± 0.14	0.19 ± 0.06	0.21 ± 0.07	0.23 ± 0.07	0.23 ± 0.07
Q	Pleiades	26.4 ± 25.5	19.0 ± 13.5	0.26 ± 0.25	0.20 ± 0.08	0.22 ± 0.08	0.23 ± 0.09	0.23 ± 0.08
	Chamelon	22.0 ± 7.0	22.0 ± 3.6	0.21 ± 0.09	0.18 ± 0.07	0.19 ± 0.07	0.21 ± 0.08	0.21 ± 0.08
R	Pleiades	24.0 ± 15.7	25.7 ± 3.3	0.53 ± 0.23	0.42 ± 0.14	0.47 ± 0.14	0.54 ± 0.15	0.54 ± 0.15
	Chamelon	25.4 ± 6.30	25.5 ± 3.1	0.45 ± 0.17	0.40 ± 0.10	0.45 ± 0.11	0.51 ± 0.11	0.54 ± 0.12
S	Pleiades	29.4 ± 22.4	24.6 ± 4.9	0.41 ± 0.28	0.28 ± 0.10	0.33 ± 0.11	0.37 ± 0.11	0.36 ± 0.12
T	Pleiades	26.4 ± 20.2	24.3 ± 14.2	0.74 ± 0.25	0.54 ± 0.17	0.61 ± 0.18	0.69 ± 0.18	0.73 ± 0.18
	Chamelon	23.1 ± 5.3	22.1 ± 2.9	0.71 ± 0.18	0.58 ± 0.12	0.64 ± 0.12	0.73 ± 0.12	0.79 ± 0.12
Y	Pleiades	31.4 ± 23.7	24.4 ± 14.2	0.45 ± 0.28	0.32 ± 0.12	0.36 ± 0.14	0.38 ± 0.15	0.37 ± 0.15

Table 2. Single scattering albedo w and photometric roughness $\overline{\theta_H}$ estimated by inversion of the Hapke model on multispectral (MS) and panchromatic (P) data. B, G, R and NIR stand for the blue, green, red and near-infrared bands of Pleiades, respectively.

On the one hand, the single scattering albedo of these sites covers the entire possible range of variation (from 0.21 to 0.93). The high values ($w > 0.8$) retrieved in sites F and H, the brightest

surfaces, are close to values found over snowy surfaces or on icy satellites (Verbiscer et al., 2013). The synthetic tests showed a trend to overestimate this parameter, despite a good constraint brought by the *a posteriori* PDF. It is therefore likely that the true value of w is less than that estimated. However, the relative values are coherent: the sites made of blocks and slabs of basaltic lava flows (B, M, and Q) are the darkest ($w < 0.4$), those made of granular deposits and boulders on sedimentary deposits (A, E, I, R, and S) are moderately bright ($0.4 < w < 0.6$), and those made of clay, salt and limestones (F, H, and T) are the brightest ($w > 0.6$). As for the spectral evolution of w, it agrees with previous studies (e.g., Johnson et al., 2006a,b; Chappell et al., 2009; Wu et al., 2009; Sato et al., 2014). Fig. 12a shows the very good agreement between the single scattering albedo estimated from Pleiades and *in situ* Chamelon instrument. This is not surprising since the geometric correction parameter r has been chosen so as to minimize the residual error between the Chamelon and Pleiades data.

On the other hand, the retrieved values of $\overline{\theta_H}$ fluctuate between 15° and 35°. These values do not appear to reflect the relatively wide range and increasing macroscopic roughnesses observed in Fig. 2. For instance, the photometric roughness of site F might be expected much lower than that of site Q, which is not the case. Fig. 12b shows that the photometric roughness derived either from space or *in situ* coincides for almost all the sites, except for sites F and M. In the first case, the value estimated from the Pleiades data is larger, and in the second, it is lower. These discrepancies lie in a poor adjustment of the Hapke model illustrated by larger root-mean-square errors for sites F and M than for the other sites.

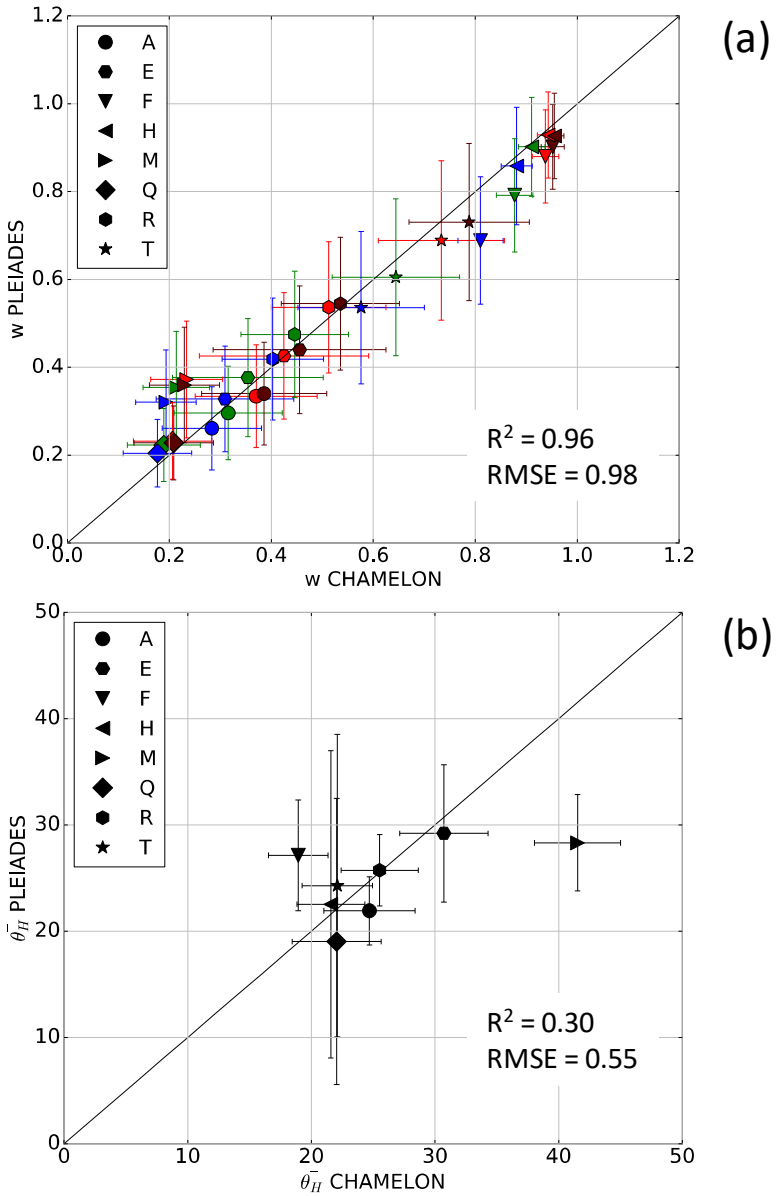


Fig. 12. Comparison of the photometric parameters estimated by Bayesian inversion of the Hapke model on the Pleiades and Chamelon data. (a) Single scattering albedo (blue, green, red and violet colors represent the four Pleiades spectral bands) and (b) Photometric roughness.

5. Discussion

The equivalence between the photometric roughness $\overline{\theta_H}$ estimated by inversion of the Hapke model and the mean roughness $\overline{\theta}$ measured in the field is not straightforward (Tables 1 and 2, Fig. 13). The former integrates all scales from the sub-millimeter scale to the decimeter scale, while the latter is derived from the slope distribution at the smallest DEM scale (~3 mm), assumed to be Gaussian. In most cases, the error bars are compatible with the hypothesis that $\overline{\theta_H} = \overline{\theta}$. Among the sites providing an error lower than 25%, one can differentiate three groups:

- Sites A and S that are smooth surfaces consisting of centimetric grains, with similar mean roughness ($\overline{\theta} = 18.57°$ for site A and $\overline{\theta} = 18.31°$ for site S). The uncertainty on $\overline{\theta_H}$ is less than 16%.
- Sites E, I, R, and T that are made of centimetric to decimetric blocks. The *a posteriori* error on the photometric roughness is more significant, but the correspondence is very good for sites I, R and T. Sites E and R have a very close spatial structure (slag deposits on lacustrine sediments, Fig. 2) leading to similar $\overline{\theta}$ values. However, the difference between $\overline{\theta_H}$ and $\overline{\theta}$ for site E is slightly larger.
- Site H that corresponds to the salt lake with a granular structure and optical properties deviating from those of rocky terrain. The uncertainty on the $\overline{\theta_H}$ estimate is very large.

The retrieval is poor for sites B (ropy pahoehoe lava), Q (basalt porphyry lava), F (clay deposits), Y (hyaloclastic projections) and M (cracked lava crust). The estimated photometric roughnesses is similar for sites B and Q that are comparable in terms of visual aspect of surface roughness. As far as the Chamelon is concerned, the photometric roughness and the mean roughness measured in the field agree well for moderate roughness (sites A, E, H, R, and T) with a relative error of 17.2%. The absence of correlation for sites F, M and Q still comes out.

The sources of discrepancy are difficult to identify. The Orfeo ToolBox used for the atmospheric correction, assumes that the surface is Lambertian, which is naturally wrong in nature and may affect the calculation of the reflectance (e.g., Lyasputin, 1999; Li et al., 2010; Ceamanos et al., 2013). The effect of the local topography can be also accounted for but we ignored it here because the surfaces studied are nearly flat. Li et al. (2012) highlighted the effectiveness of these two corrections on Landsat temporal data. Therefore, it is likely that an approximate atmospheric correction based on Lambertian assumptions has an impact on the estimation of surface roughness, especially at grazing viewing angles.

The estimation of surface roughness through photometric roughness seems to be satisfactory on surfaces displaying granular structures, the size of which is greater than a centimeter, or small blocks.

460 In the case of finer-grained surfaces or more complex structures (slabs, fractures, depressions), the
461 Hapke model fits the observations but the roughness estimates are biased. The performance of the
462 inversion may be poor if the surface departs too much from the hypotheses of the Hapke model.
463 Moreover, the photometric roughness that measures shading at the particle scale is supposed to also
464 depend on the transparency of the particles and their scattering behavior (e.g., Shepard and Campbell,
465 1998; Cord et al., 2003; Pilorget et al., 2016). Finally, the Hapke model considers a collimated
466 incident light while the atmospheric scattering makes the sun light a spread source for terrestrial
467 surfaces. This tends to reduce the shadowing on the surface and to underestimate the photometric
468 roughness. Note that the part of the reflectance due to diffuse light is still a pending question on soils,
469 while it has been quantified for a long time on vegetation. Last but not least, Labarre et al. (2017)
470 showed that the photometric roughness was controlled by the smallest scales of the surface. Thus, it is
471 likely that this parameter is sensitive to scales smaller than the scale of the DEMs produced in this
472 study for the computation of the mean roughness parameter. This would result in an underestimation
473 of $\overline{\theta}$, in particular for the smoothest surfaces.
474

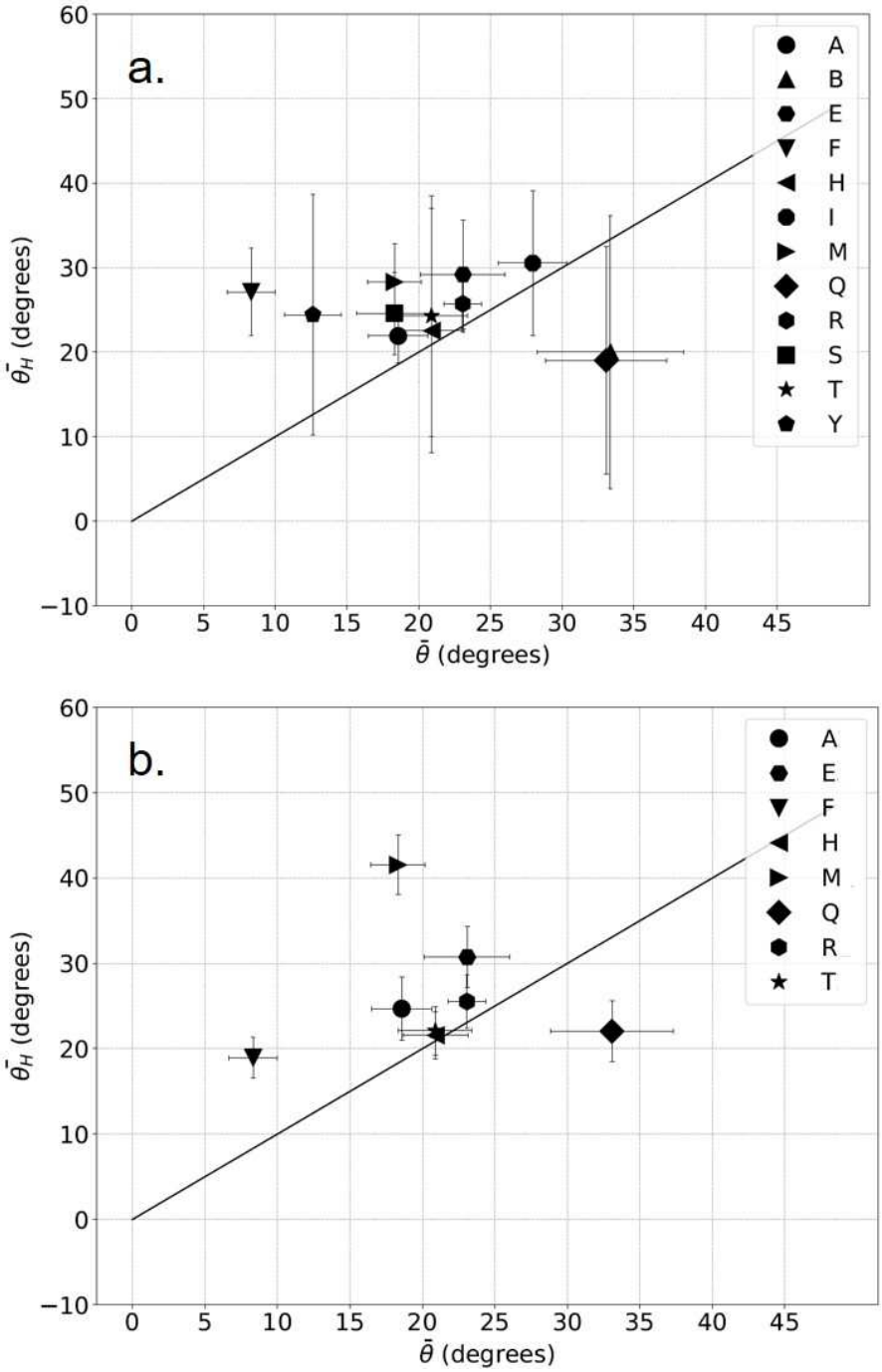


Fig. 13. Estimated photometric roughness $\overline{\theta_H}$ as a function of the measured mean roughness $\overline{\theta}$ for 12 sites (see Fig. 2) from (a) Pleiades data and (b) Chamelon data.

6. Conclusion

We have investigated the capacity of the Hapke model to retrieve the surface roughness of bare soils from multiangular reflectance data. This model is indeed commonly used in planetary science even if its validation is still an open issue. We aimed at coupling *in situ* measurements on bare soils with remote multiangular observations at high resolution to address this issue or show the potentials and limits of these data and method. Because of its agility and spatial resolution, the Pleiades satellite

was able to measure angular reflectance of natural surfaces of reduced extend and wide diversity, from space, from a large number of viewing angles, which, with a few exceptions is unique on Earth remote sensing. If performant this model would provide a new physical description of bare soils with many derived applications.

For the first time we measured the topography of large areas (~20 m × 20 m) at the millimeter scale, determined their surface roughness defined as the mean slope angle, and tried to relate the photometric roughness as derived from to multi-angular optical data acquired in the field of from space. We showed that the atmospheric correction is critical to estimate surface roughness, due to the strong influence of aerosols but also of the adjacency effect on the shape and amplitude of the bidirectional reflectance. Part of this issue was solved by cross-calibrating remote and *in situ* observations in R,G B and IR bands. We emphasized that the Lambertian assumption enclosed in the software used for the atmospheric correction may have an impact on the results. A Bayesian inversion of the Hapke model was conducted to cope with the non-linearity of the model and to assess the uncertainties associated with parameter estimation. Two approaches were explored: the first one consisting of a simultaneous inversion on the four Pleiades bands, assuming that the single scattering albedo is the only wavelength-dependent parameter, and the second one consisting of an inversion on the panchromatic band. Results were found better in the first case, with greatly reduced uncertainties on the parameters, because of better observational constraints.

This study revealed that the coherence between the photometric roughness $\overline{\theta_H}$ and the mean roughness $\overline{\theta}$ was good for moderately rough surfaces presenting homogeneous granular structures, but poor for solid floor areas or highly rough surfaces presenting more complex structures (slabs, hollows, fractures), which do not fit Hapke model hypothesese. This article is the result of an exploratory work and provides a framework to scientists wishing to estimate surface roughness using optical remote sensing. Other experiments will be required at different scales, including the topographic one, before we totally understand the determinism of soil bidirectional reflectance.

Acknowledgments

The PhD thesis of Sébastien Labarre was funded by the Direction Générale de l'Armement (DGA) and by the Commissariat à l'Energie Atomique et aux Energies Alternatives (CEA). Field data were acquired in the frame of the CAROLInA (*Characterization of Multi-Scale Roughness using OpticaL ImAgery*) project funded by CNES. The authors would like to thank Sophie Lachérade (CNES) and Claire Tinel (CNES) who enabled us to acquire the Pleiades images, Jean-Bernard de Chabalier (IPGP) who guided part of the team in the Asal-Ghoubbet rift during the exploratory mission in April 2015, Hélène Robic (IPGP), Michel Diament (IPGP) and Yann Klinger (IGGP) for their invaluable help, the CERD team who provided us logistical assistance on the ground. Fig. 1 contains modified Copernicus Sentinel data 2018, processed by ESA.

Appendix A. Calibration and atmospheric corrections

The calibration and atmospheric correction of the Pleiades images follow the four steps illustrated in Fig. 8. First the numerical value X_k recorded in band k is converted to spectral radiance $[W.m^{-2}.sr^{-1}.\mu m^{-1}]$ according to

$$I_{k,TOA} = \frac{X_k}{\alpha_k} + \beta_k \quad \text{(A1)}$$

where $I_{k,TOA}$ is the radiance measured at the top of the atmosphere, α_k is the absolute calibration gain, and β_k is the absolute calibration bias. These two parameters are contained in the metadata. The radiance value can be then converted into a TOA reflectance factor:

$$\rho_{k,TOA} = \frac{\pi I_{k,TOA} {d_0}^2}{J_{k,i}\,\mu_0} \quad \text{(A2)}$$

with $J_{k,i}$ the solar illumination at the upper limit of the atmosphere for the Earth-Sun distance d_0 expressed in astronomical units, at the date of acquisition. In order to calculate the surface reflectance,

one needs to provide the atmospheric pressure P_a $[hPa]$, the water vapor content U_{H_2O} $[g.cm^{-2}]$, the ozone content U_{O_3} [DU], the aerosol optical thickness τ_A at 550 nm, a predefined aerosol model (desert) to determine the aerosol phase function P_A and the single scattering albedo ω_0, as well as sensor intrinsic parameters (solar and viewing zenith and azimuth angles, acquisition date, sensor spectral response at a given wavelength).

Gases and aerosols are the two major atmospheric constituents causing the extinction of solar radiation by absorption or scattering. According to Vermote et al. (1997), the TOA reflectance factor of a uniform and Lambertian surface illuminated with an incidence angle i and observed at a viewing angle e, is written as

$$\rho_{TOA} = \rho_{atm} + T(i)T(e)\frac{\rho_t}{1-\rho_t S} \tag{A3}$$

with ρ_{atm} the intrinsic atmospheric reflectance factor, $T(i)$ and $T(e)$ the total atmospheric transmittances in the illumination (i) and viewing (e) directions, ρ_t the reflectance factor of the target, and S the atmospheric spherical albedo. Taking explicitely into account absorption by water vapor and ozone, the TOA reflectance factor ρ_{TOA} at a given wavelength becomes:

$$\begin{aligned}\rho_{TOA}(i,e,\phi,P_a,\tau_A,\omega_0,P_A,U_{H_2O},U_{O_3}) \\ = T(i,e,\phi,P_a,U_{O_3})\Big[\rho_{atm}\big(i,e,\phi,P_a,\tau_A,\omega_0,P_A,U_{H_2O}\big) \\ + T_{atm}(i,e,\phi,P_a,\tau_A,\omega_0,P_A)\frac{\rho_t}{1-\rho_t S(P_a,\tau_A,\omega_0,P_A)}T_{H_2O}\big(i,e,U_{H_2O}\big)\Big]\end{aligned} \tag{A4}$$

with U_{H_2O} the total atmospheric water vapor content $[g.cm^{-2}]$, U_{O_3} the total column ozone content [DU], T_{H_2O} the transmittance of atmospheric water vapor, T the transmittance of all other gases, T_{atm} the total atmospheric transmittance, $\phi = \phi_e - \phi_i$ the relative azimuth angle, P_a the atmospheric pressure $[hPa]$, τ_A the aerosol optical thickness, ω_0 the aerosol single scattering albedo, and P_A the aerosol phase function.

To take into account the nonuniformity of the surface, the average reflectance $\langle\rho\rangle$ of the pixels surrounding the target pixel is computed as (Vermote et al., 1997):

$$\langle\rho\rangle = \int_0^{2\pi}\int_0^{\infty} \rho'(r,\psi)\, F(r)\, d\psi\, dr \tag{A5}$$

with $F(r)$ the environmental function (probability that a photon incident on the target be scattered and impacts the surface within a circle of radius r around the target center) and $\rho'(r,\psi)$ the surface reflectance in polar coordinates. The boundary conditions are $F(0) = 0$ and $F(\infty) = 1$. $F(r)$ is a complex function of the molecule and aerosol phase function, their optical thickness and vertical distribution. Their contribution can be taken into account separately:

$$F(r) = \frac{t_d^R(e)\, F_R(r) + t_d^A(e)\, F_A(r)}{t_d(e)} \tag{A6}$$

with $t_d^R(\mu)$ and $t_d^A(\mu)$ the diffuse transmission factors for molecules and aerosols. Finally, the surface reflectance ρ_c is expressed as

$$\rho_c = \frac{\rho_t T(e) - \langle\rho\rangle t_d(e)}{e^{-\tau/\mu}} \tag{A7}$$

where $t_d(e)$ is the diffuse transmittance factor in the viewing direction, τ is the atmospheric optical thickness and $\mu = \cos e$.

Appendix B. Shadowing function

The shadowing function used in Eq. (2) is detailed in Hapke (2012). There are two different ways of calculating it:

$$S\left(i,e,g,\overline{\theta_H}\right)_{i\le e} = \frac{\mu_e}{\eta(e)}\frac{\mu_0}{\eta(i)}\frac{\chi\left(\overline{\theta_H}\right)}{1-f(\phi)+f(\phi)\chi(\overline{\theta_H})[\mu_0/\eta(i)]} \quad \text{(B1)}$$

$$S\left(i,e,g,\overline{\theta_H}\right)_{i>e} = \frac{\mu_e}{\eta(e)}\frac{\mu_0}{\eta(i)}\frac{\chi\left(\overline{\theta_H}\right)}{1-f(\phi)+f(\phi)\chi(\overline{\theta_H})[\mu/\eta(e)]} \quad \text{(B2)}$$

578

579 with i and e are the illumination and viewing angles, $\overline{\theta_H}$ is the photometric roughness, $\mu_0 = \cos i$,

580 $\mu = \cos e$, and μ_e is the cosine of the effective viewing angle. The functions χ, η and f are written as

581

$$\chi\left(\overline{\theta_H}\right) = \frac{1}{1+\pi\, tan^2\left(\overline{\theta_H}\right)} \quad \text{(B3)}$$

$$\eta(x) = \chi(\overline{\theta_H})\left[\cos(x)+\sin(x)\tan(\overline{\theta_H})\frac{E_2(x)}{2-E_1(x)}\right] \quad \text{(B4)}$$

$$f(\phi) = exp\left(-2\,tan\left(\frac{\phi}{2}\right)\right) \quad \text{(B5)}$$

582

583 with

584

$$E_1(x) = exp\left(-\frac{2}{\pi}cot\left(\overline{\theta_H}\right)cot(x)\right) \quad \text{(B6)}$$

$$E_2(x) = exp\left(-\frac{1}{\pi}cot^2\left(\overline{\theta_H}\right)cot^2(x)\right) \quad \text{(B7)}$$

585

586 **References**

587 Antonenko I. and Osinki G.R. (2010), Automated detection of basalt spectra in Clementine Lunar data, In *Proc.*
588 *41st Lunar and Planetary Science Conference*, pp. 26–27.
589 Bachmann C.M., Abelev A., Montes M.J., Philpot W., Gray D., Doctor K.Z., Fusina R.A., Mattis G., Chen W.,
590 Noble S.D., Coburn C., Corl T., Slomer L., Nichols C.R., van Roggen E., Hughes R.J., Carr S., Kharabash
591 S., Brady A. and Vermillion M. (2016), Flexible field goniometer system: the Goniometer for Outdoor
592 Portable Hyperspectral Earth Reflectance, *Journal of Applied Remote Sensing*, 10(3):036012.
593 Beck P., Pommerol A., Thomas N., Schmitt B., Moynier F. and Barrat J.A. (2012), Photometry of meteorites,
594 *Icarus*, 218(1):364–377.
595 Bretar F., Arab-Sedze M., Champion J., Pierrot-Deseilligny M., Heggy E. and Jacquemoud S. (2013), An
596 advanced photogrammetric method to measure surface roughness: application to volcanic terrains in the
597 Piton de la Fournaise, Reunion Island, *Remote Sensing of Environment*, 135:1–11.
598 Caminiti A.M. (2000), *Le fossé d'Asal et le lac Abhé. Deux sites géologiques exceptionnels en République de*
599 *Djibouti*, Editions Couleur Locale, 128 pp.
600 Chappell A., Zobeck T.M. and Brunner G. (2006), Using bi-directional soil spectral reflectance to model soil
601 surface changes induced by rainfall and wind-tunnel abrasion, *Remote Sensing of Environment*, 102(3–
602 4):328–343.
603 Chappell A., Leys J.F., McTainsh G.H., Strong C. and Zobeck T.M. (2009), Simulating Multi-angle Imaging
604 Spectro-Radiometer (MISR) sampling and retrieval of soil surface roughness and composition changes
605 using a bi-directional soil spectral reflectance model, in *Recent Advances in Remote Sensing and*
606 *Geoinformation Processing for Land Degradation Assessment* (Roeder A. & Hill J., eds), Taylor &
607 Francis, pp.243–259.
608 Cierniewski J. (1987), A model for soil surface roughness influence on the spectral response of bare soil in the
609 visible and near-infrared range, *Remote Sensing of Environment*, 23(1):97–115.
610 Cord A., Pinet P., Daydou Y. and Chevrel S. (2003), Planetary regolith surface analogs: optimized

611 determination of Hapke parameters using multi-angular spectro-imaging laboratory data, *Icarus*, 165(2),
612 pp.414–427.
613 Despan D., Bedidi A. and Cervelle B. (1999), Bidirectional reflectance of rough bare soil surfaces, *Geophysical*
614 *Research Letters*, 26(17):2777–2780.
615 Doctor K.Z., Bachmann C.M., Gray D.J., Montes M.J. and Fusina R.A. (2015), Wavelength dependence of the
616 bidirectional reflectance distribution function (BRDF) of beach sands, *Applied Optics*, 54(31):F243.
617 Fernando J., Schmidt F., Pilorget C., Pinet P., Ceamanos X., Douté S., Daydou Y. and Costard F. (2015),
618 Characterization and mapping of surface physical properties of Mars from CRISM multi-angular data:
619 application to Gusev Crater and Meridiani Planum, *Icarus*, 253:271–295.
620 Furey J. (2016), Laboratory goniometer approach for spectral polarimetric directionality, In *Proc. Polarization:*
621 *Measurement, Analysis, and Remote Sensing XII* (Chenault D.B. & Goldstein D.H., eds), Baltimore, MD,
622 USA, 17 April 2016, SPIE, Vol. 9853, pp. 98530I.
623 Gleyzes M.A., Perret L. and Kubik P. (2012), Pleiades system architecture and main performances, in
624 *International Archives of the Photogrammetry, Remote Sensing and Spatial Information Sciences*, *XXII*
625 *ISPRS Congress*, 25 August - 01 September 2012, Melbourne, Australia, Vol. XXXIX-B1, pp. 537–542.
626 Gunderson K., Thomas N. and Whitby J.A. (2006), First measurements with the Physikalisches Institut
627 Radiometric Experiment (PHIRE), *Planetary and Space Science*, 54(11):1046–1056.
628 Hapke B. (1981), Bidirectional reflectance spectroscopy: 1. Theory, *Journal of Geophysical Research: Solid*
629 *Earth*, 86(B4):3039–3054.
630 Hapke B. (1984), Bidirectional reflectance spectroscopy: 3. Correction for macroscopic roughness, *Icarus*,
631 59(1):41–59.
632 Hapke B. (2008), Bidirectional reflectance spectroscopy: 6. Effects of porosity, *Icarus*, 195(2):918–926.
633 Hapke B. (2012), *Theory of Reflectance and Emittance Spectroscopy*, Cambridge University Press, 528 pages.
634 Harms J.D., Bachmann C.M., Faulring J.W. and Ruiz Torres A.J. (2016), A next generation field-portable
635 goniometer system. In *Proc. Algorithms and Technologies for Multispectral, Hyperspectral, and*
636 *Ultraspectral Imagery XXII* (Velez-Reyes M. & Messinger D.W., eds), Baltimore, MD, USA, 17 April
637 2016, SPIE, Vol. 9840, pp. 98400J.
638 Helfenstein P. and Shepard M.K. (1999), Submillimeter-scale topography of the Lunar regolith, *Icarus*,
639 141(1):107–131.
640 Helfenstein P. and Shepard M.K. (2011), Testing the Hapke photometric model: improved inversion and the
641 porosity correction, *Icarus*, 215(1):83–100.
642 Irons J.R., Campbell G.S., Norman J.M., Graham D.W. and Kovalick W.M. (1992), Prediction and
643 measurement of soil bidirectional reflectance, *IEEE Transations on Geoscience and Remote Sensing*,
644 30(2):249–260.
645 Jacquemoud S., Baret F. and Hanocq J.F. (1992), Modeling spectral and bidirectional soil reflectance, *Remote*
646 *Sensing of Environment*, 41(2–3):123–132.
647 Johnson J.R., Grundy W.M., Lemmon M.T., Bell J.F., Johnson M.J., Deen R., Arvidson R.E., Farrand W.H.,
648 Guinness E.A., Hayes A.G., Herkenhoff K.E., Seelos F., Soderblom J. and Squyres S. (2006a),
649 Spectrophotometric properties of materials observed by Pancam on the Mars Exploration Rovers: 1.
650 Spirit, *Journal of Geophysical Research: Planets*, 111(E2):E02S14.
651 Johnson J.R., Grundy W.M., Lemmon M.T., Bell J.F., Johnson M.J., Deen R., Arvidson R.E., Farrand W.H.,
652 Guinness E.A., Hayes A.G., Herkenhoff K.E., Seelos F., Soderblom J. and Squyres S. (2006b),
653 Spectrophotometric properties of materials observed by Pancam on the Mars Exploration Rovers: 2.
654 Opportunity, *Journal of Geophysical Research: Planets*, 111(E12):E12S16.
655 Johnson J.R., Shepard M.K., Grundy W.M., Paige D.A. and Foote E.J. (2013), Spectrogoniometry and
656 modeling of martian and lunar analog samples and Apollo soils, *Icarus*, 223(1):383–406.
657 Labarre S., Ferrari C. and Jacquemoud S. (2017), Surface roughness retrieval by inversion of the Hapke model:
658 a multiscale approach, *Icarus*, 290:63–80.
659 Lachérade S., Fourest S., Gamet P. and Lebègue L. (2012), Pleiades absolute calibration: inflight calibration
660 sites and methodology, in *ISPRS International Archives of the Photogrammetry, Remote Sensing and*
661 *Spatial Information Sciences*, XXXIX-B1, pp.549–554.
662 Li F., Lymburner L., Mueller N., Tan P., Islam A., Jupp D.L.B. and Reddy S. (2010), An evaluation of the use
663 of atmospheric and BRDF correction to standardize Landsat data, *IEEE Journal of Selected Topics in*
664 *Applied Earth Observations and Remote Sensing*, 3(3):257–270.
665 Li F., Jupp D.L.B., Thankappan M., Lymburner L., Mueller N., Lewis A. and Held A. (2012), A physics-based
666 atmospheric and BRDF correction for Landsat data over mountainous terrain, *Remote Sensing of*
667 *Environment*, 124:756–770.
668 Lumme K. and Bowell E. (1981), Radiative transfer in the surfaces of atmosphereless bodies. I. Theory,

669 *Astronomical Journal*, 86(11):1694-1721.
670 Lyasputin A.I. (1999). Atmospheric and geometrical effects on land surface albedo, *Journal of Geophysical*
671 *Research: Atmospheres*, 104(D4):4127–4143.
672 McGuire A.F. and Hapke B.W. (1995), An experimental study of light scattering by large irregular particles,
673 *Icarus*, 113(1):134-155.
674 Patil A. (2010), PyMC: Bayesian stochastic modelling in Python, *Journal of Statistical Software*, 35(4):1–81.
675 Pierrot-Deseilligny M. and Paparoditis N. (2006), A multiresolution and optimization-based image matching
676 approach: an application to surface reconstruction from SPOT5-HRS stereo imagery, In Proc.
677 *Topographic Mapping from Space (with Special Emphasis on Small Satellites)*, 14-16 February 2006,
678 Ankara, Turkey, ISPRS Archives, Vol. XXXVI-1/W41, 5 pp.
679 Pilorget C., Fernando J., Ehlmann B.L., Schmidt F. and Hiroi T. (2016), Wavelength dependence of scattering
680 properties in the VIS-NIR and links with grain-scale physical and compositional properties, *Icarus*,
681 267:296–314.
682 Pinty B., Verstraete M.M. and Dickinson R.E. (1989), A physical model for predicting bidirectional
683 reflectances over bare soil, *Remote Sensing of Environment*, 27(3):273–288.
684 Pinzuti P., Humler E., Manighetti I. and Gaudemer Y. (2013), Petrological constraints on melt generation
685 beneath the Asal Rift (Djibouti) using quaternary basalts, *Geochemistry, Geophysics, Geosystems*,
686 14(8):2932–2953.
687 Pommerol A., Thomas N., Jost B., Beck P., Okubo C. and McEwen A.S. (2013), Photometric properties of
688 Mars soils analogs, *Journal of Geophysical Research: Planets*, 118(10):2045–2072.
689 Rupnik E., Daakir M. and Pierrot-Deseilligny M. (2017), MicMac – a free, open-source solution for
690 photogrammetry, *Open Geospatial Data, Software and Standards*, 2:14.
691 Rupnik E., Pierrot-Deseilligny M. and Delorme A. (2018), 3D reconstruction from multi-view VHR-satellite
692 images in MicMac, ISPRS Journal of Photogrammetry and Remote Sensing, 139:201–211.
693 Sandmeier S.R. (2000), Acquisition of bidirectional reflectance factor data with field goniometers, *Remote*
694 *Sensing of Environment*, 73(3):257–269.
695 Sato H., Robinson M.S., Hapke B., Denevi B.W. and Boyd A.K. (2014), Resolved Hapke parameter maps of
696 the Moon, *Journal of Geophysical Research: Planets*, 119(8):1775–1805.
697 Schaepman-Strub G., Schaepman M.E., Painter T.H., Dangel S. and Martonchik J.V. (2006), Reflectance
698 quantities in optical remote sensing—definitions and case studies, Remote Sensing of Environment,
699 103(1):27-42.
700 Schmidt F. and Fernando J. (2015), Realistic uncertainties on Hapke model parameters from photometric
701 measurement, *Icarus*, 260:73–93.
702 Shepard M.K. and Campbell B.A. (1998), Shadows on a planetary surface and implications for photometric
703 roughness, *Icarus*, 134(2):279–291.
704 Shepard M.K. and Helfenstein P. (2007), A test of the Hapke photometric model, *Journal of Geophysical*
705 *Research: Planets*, 112(E3):E03001.
706 Shepard M.K. and Helfenstein P. (2011), A laboratory study of the bidirectional reflectance from particulate
707 samples, *Icarus*, 215(2):526–533.
708 Shkuratov Y., Starukhina L., Hoffmann H. and Arnold G. (1999), A model of spectral albedo of particulate
709 surfaces: implications for optical properties of the Moon, *Icarus*, 137:235–246.
710 Shkuratov Y. and Helfenstein P. (2001), The opposition effect and the quasi-fractal structure of regolith: I.
711 Theory, *Icarus*, 152(1):96–116.
712 Souchon A.L., Pinet P.C., Chevrel S.D., Daydou Y.H., Baratoux D., Kurita K., Shepard M.K. and Helfenstein
713 P. (2011), An experimental study of Hapke's modeling of natural granular surface samples, *Icarus*,
714 215(1):313–331.
715 Staid M. (2000), Integrated spectral analysis of Mare soils and craters: applications to eastern nearside basalts,
716 *Icarus*, 145(1):122–139.
717 Stieltjes L. (1980), Carte géologique du rift d'Asal 1/50 000 (Dépression Afar, est-africain. République de
718 Djibouti), CNRS Editions, Paris.
719 Verbiscer A.J., Helfenstein P. and Buratti B.J. (2013), Photometric properties if Solar System ices, in *The*
720 *Science of Solar System Ices* (Gudipati M.S. & Castillo-Rogez J., eds), Springer, pp.47–72.
721 Vermote E., Tanré D., Deuzé J.L., Herman M. and Morcrette J.J. (1997), Second Simulation of the satellite
722 signal in the solar spectrum (6S): an overview, *IEEE Transactions on Geoscience and Remote Sensing*,
723 35:675–686.
724 Vincendon M. (2013), Mars surface phase function constrained by orbital observations, *Planetary and Space*
725 *Science*, 76(1):87–95.
726 Wu Y., Gong P., Liu Q. and Chappell A. (2009), Retrieving photometric properties of desert surfaces in China

727 using the Hapke model and MISR data, *Remote Sensing of Environment*, 113(1):213–223.